Spring 3-11-2020

Characterization of a Trochoidal Electron Monochromator

Jesse Kruse
University of Nebraska - Lincoln

Characterization of a Trochoidal Electron Monochromator

Jesse A. Kruse

Undergraduate Thesis
University of Nebraska-Lincoln
March 2020

Faculty Advisors:
Dr. Timothy Gay
Dr. Herman Batelaan

Abstract

This thesis presents a quantitative study of a trochoidal electron monochromator and attempts to observe the $2p^5 3p^2$ resonance in neon. A detailed description of the experimental apparatus, including the electron beam system, the vacuum system, and the light analysis system, is presented first. Then, we discuss the theory of how the electron beam is monochromatized, how we measured monochomatization, and how we analyze the light being emitted from the collision cell. The light analysis system is capable of accurately measuring the relative Stokes parameters for any polarization of light, and the electron beam system is capable of producing electron beams with transmitted currents ranging from 1 nA to 500 nA with varying degrees of monochromatization. Retarding field analysis yielded substandard energy width measurements of our beam so we looked to the neon resonance as a secondary means of measurement. Despite our best efforts, we were unable to observe light from this resonance above background sources. A number of reasons are proposed to explain this failure as well as possible improvements to the experimental apparatus.

Key Words: Physics, electron, monochromator, resonance, light

Contents

1 Introduction **5**

2 Experimental Apparatus **7**

2.1 The Electron Beam System 8

2.1.1 The Electron Gun 8

2.1.2 The Monochromator 9

2.1.3 Collision Cell and Energy Analysis Sections 12

2.2 Vacuum System 12

2.3 Light Analysis System 15

3 Theory of Operation **18**

3.1 The Trochoidal Monochromator 18

3.2 Retarding Field Analysis 21

3.3 Optical Polarization Measurements 22

4 Calibration **26**

4.1 Optical Polarization Measurements 26

4.2 Production and Analysis of an Electron Beam 30

4.3 The Search for Light 38

5 Conclusions **43**

List of Figures

2.1 *Schematic diagram of the experimental setup. Abreviations "IF", "LP", and "$\lambda/4$" refer to the interference filter, linear polarizer, and quarter-wave retarder respectively. Dimensions are not to scale.* 8

2.2 *Picture of the experimental setup displaying vacuum chamber, Helmholtz coils, and lights analysis section.* 9

2.3 *Electostatic optic configuration used for generating, monochromatizing, and analyzing electron beam.* 10

2.4 *Electrode schematic of the electron beam system with labels of each element. The filament, indicated by the rotated caret, is mounted between elements M-1 and M1. Made by Will Brunner.* 10

2.5 *Diagram of the electron aperture offset for molybdenum annuli M1-M3 with relevant dimensions. Made by Will Brunner.* 11

2.6 *Wireframe potential diagram of the electron gun made with SIMION®. Electrons begin on the right and end on the left.* 11

2.7 *Circuit diagram for electron gun filament modeled after [10].* 13

2.8 *(Left) Diagram of vacuum system facing North. (Right) Diagram of 4-way cross from top-down view.* 14

2.9 *(Left) Four way cross in the foreline of the vacuum chamber. (Right) Valve manifold for controlling flow of neon gas in the vacuum system.* 15

2.10 *Schematic diagram of the light analysis system. Note, that CC, CL, QWP, LP, and IF stand for collision chamber, converging lens, quarter-wave plate, linear polarizer, and interference filter respectively. All length measurements have an uncertainty of 1 cm.* 16

2.11 *Schematic of photon detection system. The high voltage power supply for the PMT is a Pacific Instruments model 204, and the other voltages are supplied by Topward 3303A DC power supplies.* 17

3.1 *Diagram of trochoidal monochromator with relevant parameters, taken from Roy [16]. Here, v_o is the initial velocity of the electron, γ is its initial angle with respect to the z axis, D is the separation of the entrance and exit apertures in the x direction, and ΔS_1 and ΔS_2 are the entrance and exit aperture diameters respectively.* 19

3.2 *Example of a retarding field curve with derivative showing the inferred energy distribution of the electrons. Current and derivative are normalized, and the full-width-half-maximum (FWHM) is indicated in the figure.* 21

3.3 *Visual representation of the relative Stoke's parameters. Here $P_1 = M/I$, $P_2 = C/I$, and $P_3 = S/I$, where the orange P_1 is the linear polarization on the axes, the blue P_2 is canted linear polarization, and the green P_3 is the circular polarization of our light.* 22

3.4 *Diagram of elements necessary for polarization measurements, taken from [13].* 23

3.5 *Front panel of light analysis program. It was designed to display the intensity for each angle of the quarter wave plate (QWP) and, after all the data had been collected, display the measured data and the data with fit. The fit was displayed over the data as a visual check of the Fourier coefficients we calculated.* 24

4.1 *Housing for the Meadowlark quarter wave plate displaying the rotation mechanism and plunger action.* 27

4.2 *Neon discharge lamp and optical train to simulate light being emitted from collision cell for testing light analysis system. Note that a hi-tech mounting system was used for elevating the discharge lamp.* 28

4.3 *Optics setup for testing light analysis system. Convex Lens 1 had focal length of 5 cm and was positioned 5 cm away from our source to collimate the light. The adjustable iris was used to vary the intentity. Convex Lens 2 had a focal length of 31 cm and was positioned 31 cm away from the center of the collision cell so that light appeared to be originating from the collision point.* 28

4.4 *Test of Malus's Law using two linear polarizers. Top graph is measured data, and bottom graph is data with a fit.* 29

4.5 *Measurement of relative Stokes parameters for linearly polarized light as part of a test of the light analysis system.* 31
4.6 *Circuit diagram for the power supply box for the monochromator section of the electron gun. A resistor with an arrow next to it indicates a variable resistor. Voltages across variable resistors M1-7 all lead to plates M1-7 as shown in Figure 2.4.* 31
4.7 *Power supplies for controlling voltages on electrostatic elements in electron gun.* 32
4.8 *Electrical schematic for how each of the elements if connected to a voltage.* 33
4.9 *Retarding field curve for electron beam produced with initial settings.* 34
4.10 *(Left) Simulated RFA on A2 and A3 with and without a wire mesh. (Right) Distribution of electron energies at the collision cell using initial settings in Table 4.1. The data is from SIMION, and the Gaussian fit was made using Matlab.* 35
4.11 *Retarding field curve for best electron gun settings.* 36
4.12 *(Left) Simulated RFA on A2 and A3 with and without a wire mesh. (Right) Distribution of electron energies at the collision cell using best settings in Table 4.3. The data is from SIMION, and the Gaussian fit was made using Matlab.* 37
4.13 *(Left) Cross section of neon as a function of energy displaying resonances, taken from [4]. (Right) Excitation function for the* $2p^5 3p\ ^3D_3 \rightarrow 2p^5 3s\ ^3P_2$ *640.2 nm transition in neon taken from [14]. The estimated* ΔE *for the incident beam in these measurements was approximately 300 meV.* 38
4.14 *Calibration of the leak valve for metering neon into the system.* 38
4.15 *Light emitted from the hot tungsten filament as seen through the north viewport of the vacuum chamber. Heating current is approximately 5.0 A.* 40
4.16 *Intensity of light from the filament as we change heating current.* 40
4.17 *Light above background as a function of transmitted current through the electron gun.* . . . 41
4.18 *Looking for light above background as a function of voltage placed on the gas needle.* 42
4.19 *(Left) Cone preceding collimating lens for light analysis system. (Right) Electron gun from the view of the south viewport where the collimating lens cone goes.* 42

Chapter 1

Introduction

Atomic resonance studies have been a popular topic of physics research for the past century, and many pioneering physicists like George Shulz [1], Ugo Fano [2], and Herman Feshbach [3], to name a few, have classified and studied the effects of the these resonances. One can study collisional resonances using a beam of electrons, negatively ionized atoms [4], or even positrons [5]. In all of these cases, to observe the resonances and internal structures with high resolution, one must use a particle beam with a very narrow spread in energy. Most methods for achieving this "monochromatization" employ a purely electrostatic analyzer, but one can also use appropriately oriented crossed electric and magnetic fields, the classic example being the Wien filter which has both fields perpendicular to the beam trajectory and to each other.

This thesis will present a study of the trochoidal electron monochromator, which works on the basis of a longitudinal magnetic field and a transverse electric field with respect to the electron's trajectory. This type of monochromator has the capability to produce electron beams with energy widths as small as 20 meV [6], which can be applied in many different areas. A monochromatized beam of electrons is useful in the study of collisional resonances in electron-atom scattering because it allows physicists to identify closely spaced features of the atomic structure. Moreover, if the beam of electrons were spin polarized, the polarization of the photoemission following the decay of the resonance can provide additional useful information in determining the excited state.

A monochromatized beam could also allow for a more precise investigation of the work done by Maseberg et al [7]. In this work, the authors investigated the near-threshold dynamics of the $d\,^3\Pi_u \rightarrow a\,^3\Sigma_g^+$ transition in H_2 and D_2 using a spin polarized electron beam with an energy

width on the order of 400 meV [7]. With a trochoidal monochromator we could re-create this study with finer energy resolution, getting data from which we could learn much more about the physics of molecular-excitation dynamics as close as possible to the excitation threshold.

For the Accurate Electron Spin Optical Polarimeter (AESOP) project, highly accurate measurements of electron spin polarization are desired. This type of polarimeter uses the $np^5(n+1)p\ ^3D_3 \rightarrow np^5(n+1)s\ ^3P_2$ transition in heavy noble gases like neon or krypton to convert the spin polarization information into optical polarization [8]. The analyzing power of these types of polarimeters is determined by the degree of the light's linear polarization P_1, so to have a highly accurate polarimeter we need to know how this polarization changes with electron energy. With a very monochromatized beam of electrons, we can measure very precisely how P_1 varies in neon which will lead ultimately to more accurate electron polarization measurements for other experiments.

Chapter 2

Experimental Apparatus

The goals of this experiment, which can be seen schematically in Figure 2.1 and pictorially in Figure 2.2 and Figure 2.3, were to create a beam of unpolarized electrons, demonstrate monochromatization with the trochoidal monochromator, measure the excitation function of the $2p^5 3p\ ^3D_3 \rightarrow 2p^5 3s\ ^3P_2$ 640.2 nm transition in neon, resolve its large resonance near the $^3D_3$ threshold, and measure the polarization of the photoemission. To create the beam of electrons, we ran a large heating current through a tungsten filament until electrons were emitted via thermionic emission. These were then guided by a series of charged molybdenum annuli through a trochoidal monochromator to the collision cell, where the neon was injected via a tube with a high length-to-diameter ratio. There, the electrons attached themselves to the neon to form a temporary negative ion state (Ne^-) with a characteristic lifetime τ that determines the resonance width ΔE through $\Delta E * \tau \approx \hbar/2$, the energy-time form of the Heisenberg uncertainty relationship. When the negative ion state decays, the electrons depart with much less energy than they came in with (approximately 0.5 eV), and the daughter neon $^3D_3$ state emits a photon of wavelength 640.2 nm as it decays:

$$e^-(E) + Ne(2p^6) \longrightarrow Ne^-(2p^5 3p^2) \longrightarrow Ne(2p^5 3p\ ^3D_3) + e^-(E - \delta E)$$
$$\longrightarrow Ne(2p^5 3s\ ^3P_2) + \gamma(640.2nm) + e^-(E - \delta E) \quad (2.1)$$

The electrons that did not collide with the neon passed through a retarding-field analyzer before they were collected on a solid disk where we measured the current transmitted through the system.

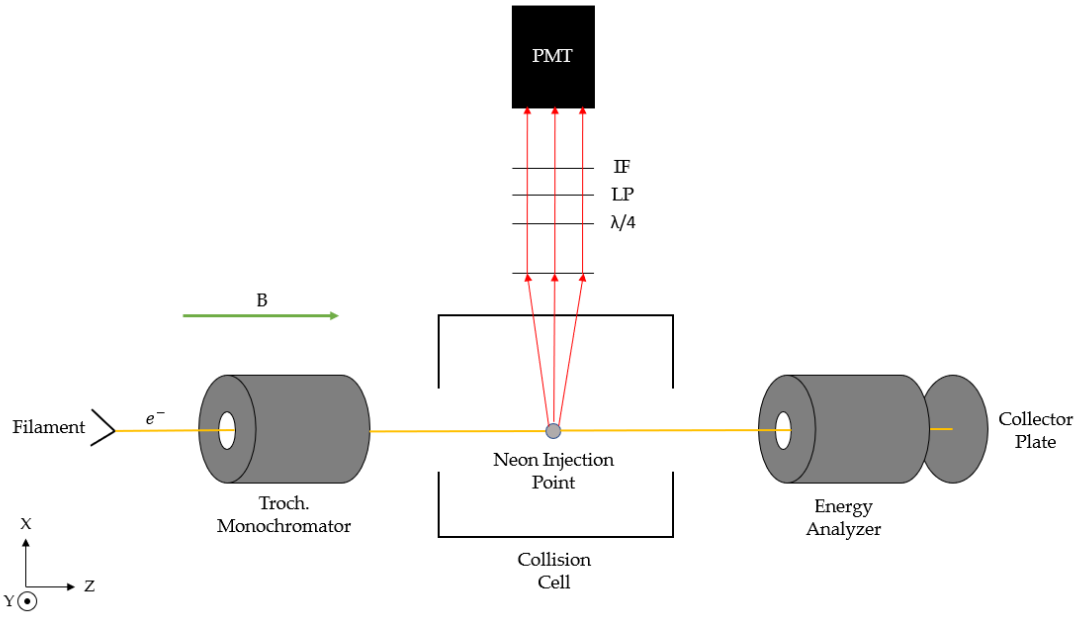

Figure 2.1: *Schematic diagram of the experimental setup. Abreviations "IF", "LP", and "λ/4" refer to the interference filter, linear polarizer, and quarter-wave retarder respectively. Dimensions are not to scale.*

2.1 The Electron Beam System

We will begin our discussion of the experimental apparatus with the source of our electrons known as the electron gun. The electron beam system in its entirety can be seen in Figure 2.3 where it was taken out of the vacuum chamber for inspection and maintenance in September of 2019. In addition a schematic with labeling conventions for each of the elements can be found in Figure 2.4.

2.1.1 The Electron Gun

The electron gun generates the electron beam by thermionic emission from a tungsten filament positioned at the top of Figure 2.3 and the left of Figure 2.4. Thermionic emission is the process by which electrons are liberated from a material because their thermal energy is enough to overcome the work function of the material. For tungsten the work function is 4.5 eV as measured by Davisson and Germer in 1902 [9]. To heat the filament, we run a current between 4 and 5.5 A through it using a Hewlett Packard 6263B DC Power Supply.

The free electrons need to be formed into a beam and directed through our vacuum chamber to the collision cell. This is achieved by the series of 1 inch diameter annuli with inner hole

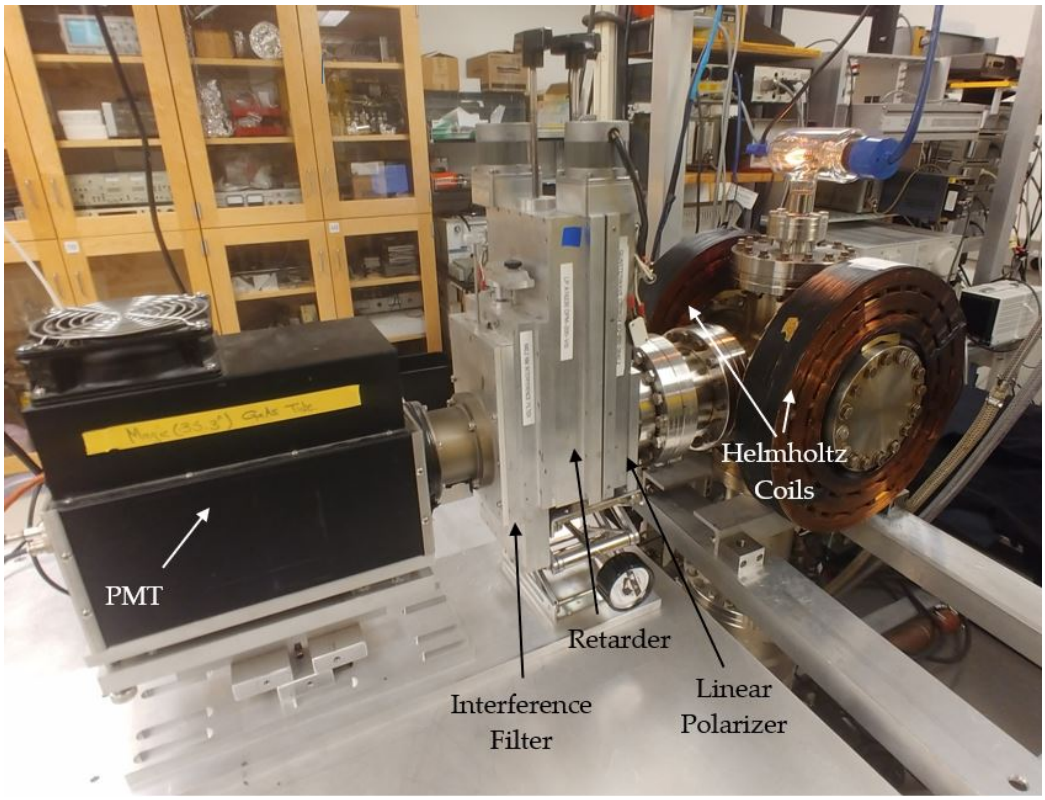

Figure 2.2: *Picture of the experimental setup displaying vacuum chamber, Helmholtz coils, and lights analysis section.*

diameters ranging from 0.035" to 0.62" (see Figure 2.4). A diagram of some of these elements and the half-cylinder "deflector" plates can be seen in Figure 2.5. The filament is floated with a negative voltage $-V_o$ using a Hewlett Packard E3611A DC power supply, and successively positive voltages are placed on the annuli downstream of the filament. This creates a potential hill for the electrons to "roll down" to the collision cell where they should have an energy of eV_o. Figure 2.6 shows a simulation of the potentials produced by the electrostatic elements in the system that was made by Will Brunner using SIMION® , an ion optics simulation program.

2.1.2 The Monochromator

When the electrons reach the trochoidal monochromator, they enter a region with an electric field transverse to their propagation in the x direction as depicted in Figure 2.1. In addition, there is an axial magnetic field of about 100 Gauss produced by two Helmholtz coils outside of the vacuum chamber. The magnetic field helps to collimate the electron beam outside of the monochromator

Figure 2.3: *Electostatic optic configuration used for generating, monochromatizing, and analyzing electron beam.*

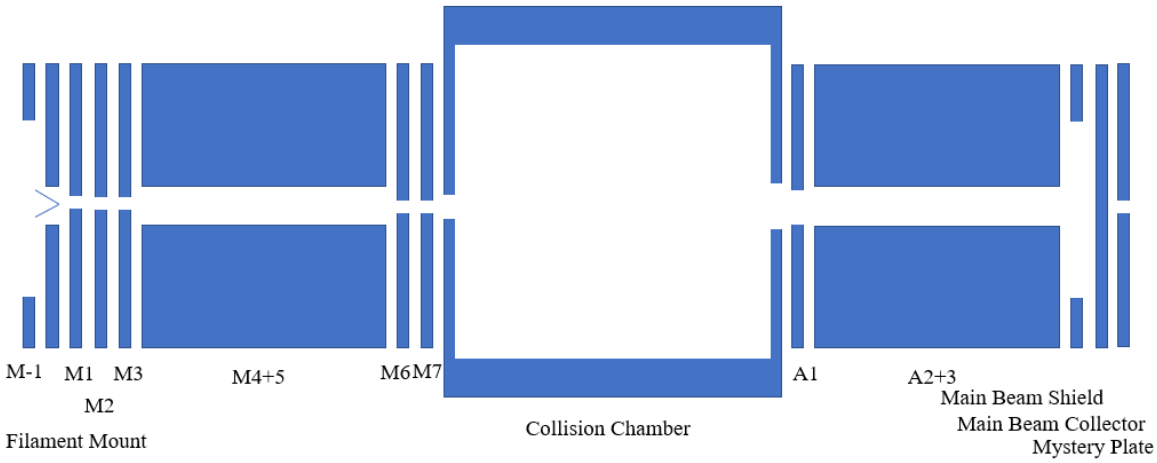

Figure 2.4: *Electrode schematic of the electron beam system with labels of each element. The filament, indicated by the rotated caret, is mounted between elements M-1 and M1. Made by Will Brunner.*

region by redirecting transverse velocity into helical motion. The principle of operation for the trochoidal monochromator relies on the crossed electric and magnetic fields. When the electrons

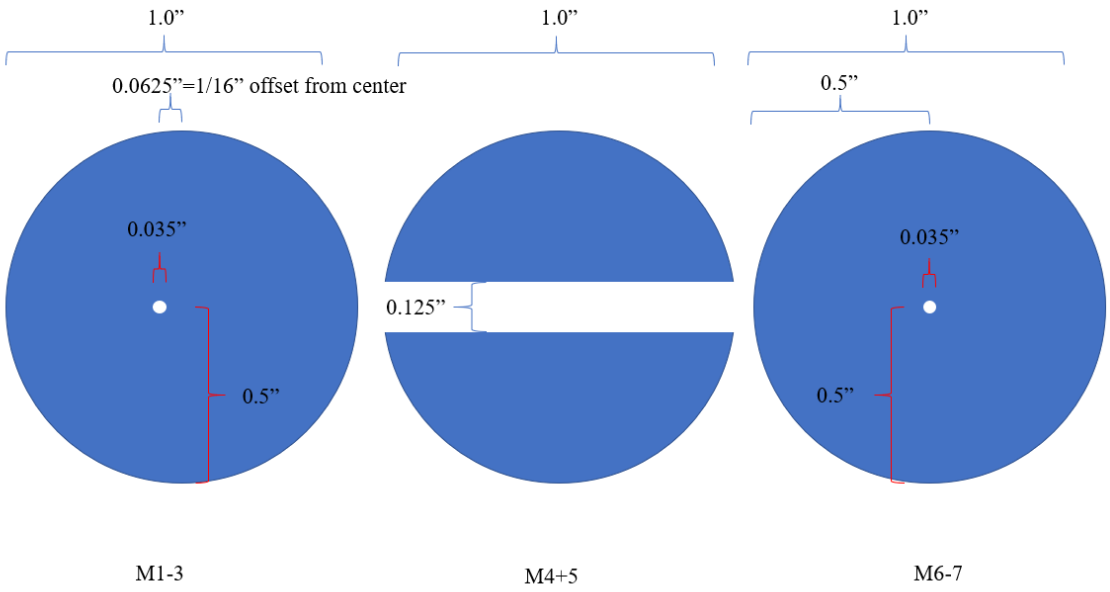

Figure 2.5: *Diagram of the electron aperture offset for molybdenum annuli M1-M3 with relevant dimensions. Made by Will Brunner.*

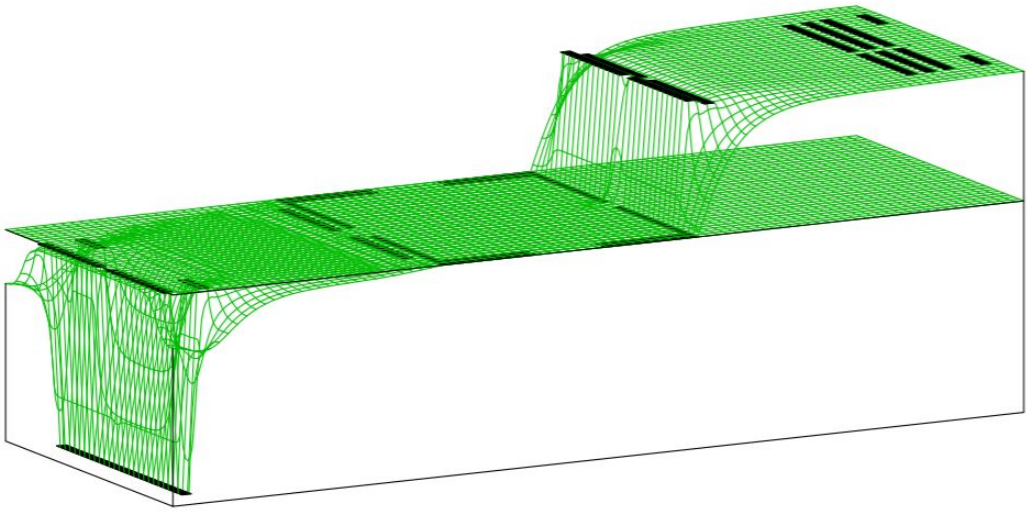

Figure 2.6: *Wireframe potential diagram of the electron gun made with SIMION®. Electrons begin on the right and end on the left.*

enter this region, they begin performing trochoidal motion and drifting in the direction according to the cross product of the $\vec{E}$ and $\vec{B}$ fields. This motion will be described in detail in the next chapter. The slower electrons spend more time in this region and therefore drift further than the faster

electrons which causes a dispersion of our beam based on kinetic energy. By carefully selecting our electric and magnetic field strengths, we can tune our monochromator to select only the electrons in a certain energy range. According to Stamatovic and Schulz, the trochoidal monochromator can achieve electron energy widths of 0.02 eV [6]. This is what we hope to ultimately achieve with this device.

2.1.3 Collision Cell and Energy Analysis Sections

After the monochromator section, the electrons accelerate to the grounded collision cell where we inject neon gas via a tube with a high length to diameter ratio. This is the interaction region where the resonance will occur and 640.2 nm light will be emitted via the $2p^5 3p\,^3D_3 \rightarrow 2p^5 3s\,^3P_2$ decay mode. The electrons leave the collision cell and enter the energy analysis section where we perform a "retarding field" analysis on them using plates A2 and A3 to define our retarding potential. After that the electrons end their flight on the main beam collector plate where we measure the current using a Keithley 614 Electrometer.

The plates labeled M1-M7 as shown in Figure 2.4 are named as such because they are a part of the monochromator section, and similarly, the plates A1-A3 are named as such because they are a part of the analysis section. The plates are electrically insulated from one another by 0.0625" diameter sapphire balls. We placed voltages on all of the elements by connecting them to their own power supplies referenced to ground. We chose to use this method over the previous voltage divider scheme because it was more intuitive and more dependable. The filament had its own special circuit, shown in Figure 2.7, where V is our HP E3611A power supply, A is our Keithley 485 picoammeter, R is a 1 MΩ resistor, and I is our HP 6263B DC power supply. We modeled it like this so that we could float the current supply and the filament by a voltage controlled by our E3611A power supply and measure the emission current from the filament at the same time. To measure the current on the main beam collector, we had to float the Keithley 614 electrometer usually to 27 V.

2.2 Vacuum System

The electron gun was carefully positioned inside a six-way cross stainless steel vacuum chamber with 6-inch Conflat® flanges shown diagramatically in Figure 2.8. The electron gun inside the

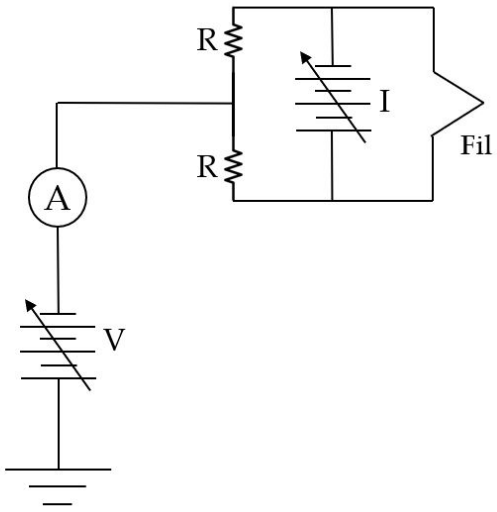

Figure 2.7: *Circuit diagram for electron gun filament modeled after [10].*

chamber is oriented east to west, and the light analysis section that will be described in the following section is oriented north-south. On the north side of the vacuum chamber, we have a 6" viewport flange so we can see the electron gun and collision cell while under vacuum. On the east side we have a blank flange, and on the west side we have the electrical feed-throughs for all of the wires connecting the electrostatic elements to their supplies and monitors. The south side of the chamber has a collimating lens viewport for the 640.2 nm light to get to the analysis section. The top of the vacuum chamber holds an Ideal Vacuum Products hot-filament ionization pressure gauge which is connected to a Granville-Phillips 307 Vacuum Gauge controller so we can monitor the pressure inside the chamber. On the bottom of the vacuum chamber we have attached a Leybold TMP-360 turbomolecular vacuum pump which spins a turbine at 45,000 rpm to compress the molecules and atoms in the chamber so that they can in turn be evacuated by a mechanical forepump [11].

In the foreline, we have attached a stainless steel 4-way cross. On the north flange of this cross, we placed a Kurt J. Lesker convectron-style pressure gauge which is also connected to our Granville-Phillips controller for display. On the south flange of this smaller cross, we have placed a valve from which we can input neon gas if we want to increase the pressure in the foreline or to quickly bring our chamber back up to atmospheric pressure. On the west flange we have connected a Welch 1397 mechanical forepump. The forepump brings our vacuum system down to the mTorr

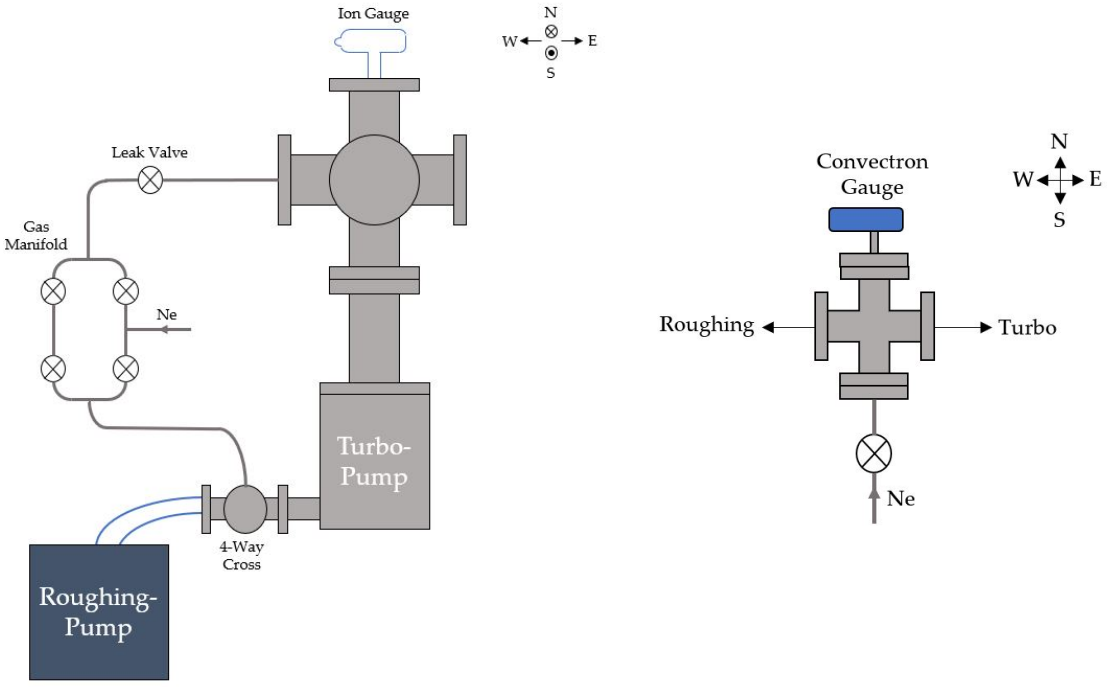

Figure 2.8: *(Left) Diagram of vacuum system facing North. (Right) Diagram of 4-way cross from top-down view.*

range (molecular flow regime) which we must do before turning on the turbomolecular pump. The Welch pump is sometimes dubbed the "roughing" pump because it provides us with a "rough" vacuum within our chamber. The nominal base pressure with the full vacuum system in operation is 2.5×10^{-9} Torr which is equivalent to 3.3×10^{-7} Pa in SI units. The base pressure was higher in the beginning of this project, but due to the heating of the filament, we baked out the vacuum chamber slightly, ridding the interior surfaces of adsorbed gases and allowing us to reach lower pressures.

To introduce neon into our vacuum chamber, we connected a large compressed gas cylinder of research grade (99.999%) neon to the manifold pictured in Figure 2.9 on the right via a length of 1/4" PTFE tubing. The two valves on the east side of the manifold allow us to flow gas to the Granville-Phillips series 203 variable leak valve or to the foreline cross as previously described. The leak valve is connected to the gas needle injector in the collision cell, and it gives us very fine control over the pressure of neon in our vacuum chamber with 270 positions between fully closed and fully open [12].

The manifold device that we have described has the capability to produce mixtures of

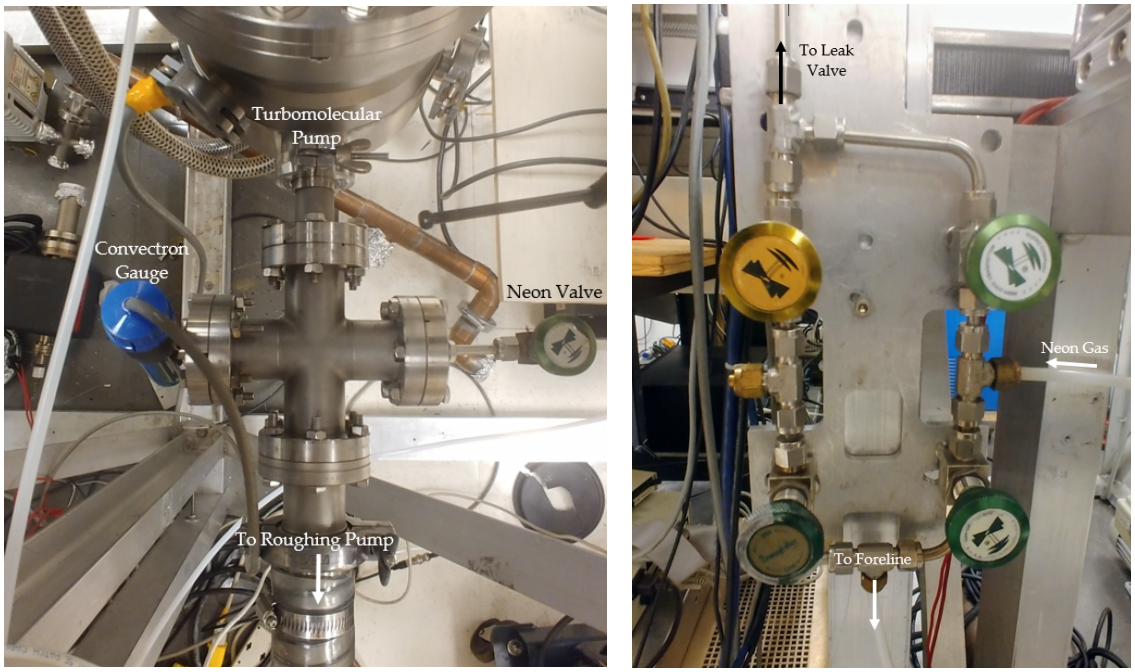

Figure 2.9: *(Left) Four way cross in the foreline of the vacuum chamber. (Right) Valve manifold for controlling flow of neon gas in the vacuum system.*

pure gases, so if we wanted to try adding a buffer gas in future studies, we could do so using this.

2.3 Light Analysis System

For a visual aid to this section, refer to Figure 2.10. After the electrons excite the neon and it decays through the $2p^5 3p\,^3D_3 \rightarrow 2p^5 3s\,^3P_2$ transition, the light produced will travel out of the collision cell's 0.275" aperture and into a collimating lens viewport on the south flange of the vacuum chamber. The lens is placed inside of a cone with an entrance aperture of 0.6875" in diameter so as to deflect light from sources other than the collision chamber. The collimating lens is positioned such that the collision volume is exactly at the lens' focal length.

Next, the light could encounter a Meadowlark NQ-200-0468 Quarter Wave Plate with a measured retardance of 1.632 rad or 0.260 waves, then a Meadowlark DPM-200-VIS linear polarizer, and then an unlabeled 640.2 nm interference filter to isolate this wavelength of light. Because the interference filter's label had been almost entirely rubbed off, we did not have the specifications or manufacturer's data on its performance. We did a quick measurement of its transmission as a function of wavelength with the help of Josh Beck in the Uiterwaal lab, and it had a peak trans-

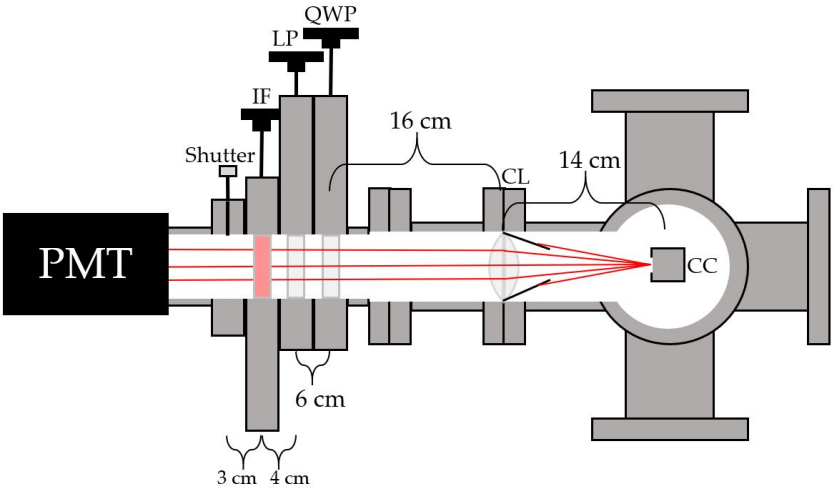

Figure 2.10: *Schematic diagram of the light analysis system. Note, that CC, CL, QWP, LP, and IF stand for collision chamber, converging lens, quarter-wave plate, linear polarizer, and interference filter respectively. All length measurements have an uncertainty of 1 cm.*

mission at 637 nm with a FWHM of 4 nm. In addition, the previous owner of the interference filter Evan Brunkow had personally labeled it as 640.2 nm, so with this information in hand, we think that the true peak wavelength of it is indeed 640.2 nm. However, it is necessary to do a more careful measurement of the transmission curve for future studies.

The quarter-wave plate, the linear polarizer, and the interference filter are all attached to individual plunger systems so they can be inserted or removed from the beam path as needed. After these three optical elements, the light is collected and converted into a photon-counting pulsed electrical signal by the Hamamatsu R943-02 photomultiplier tube (PMT). This PMT has a GaAs photocathode with a wide spectral response and was specifically selected for its low dark counts. In addition, the PMT is housed in a cooling system so we can reduce dark counts even further as they are strongly temperature dependent. We maintained the PMT temperature at -21.3 °C, where we have a measured dark count rate of 0.38(8) counts per second. Connected to the PMT, we have an Ortec VT120 fast timing preamplifier with a gain of 20. The output of the preamp is then fed into a Phillips Scientific Model 6930 Discriminator. The discriminator is set in the ΔE mode which only accepts pulses within a certain amplitude range that we can adjust, and the TTL (square wave) output of this is fed into a National Instruments 6024E Data Acquisition (DAQ) card that we can control using LabVIEW. A schematic of this system can be seen below in Figure 2.11. To take intensity measurements of the light coming from the collision cell, we created a simple counting

program that recored the number of counts and divided by the total acquisition time. Because the counting statistics are Poissonian in nature, the uncertainty in our count rate was the square root of the total number of counts, divided by the total time.

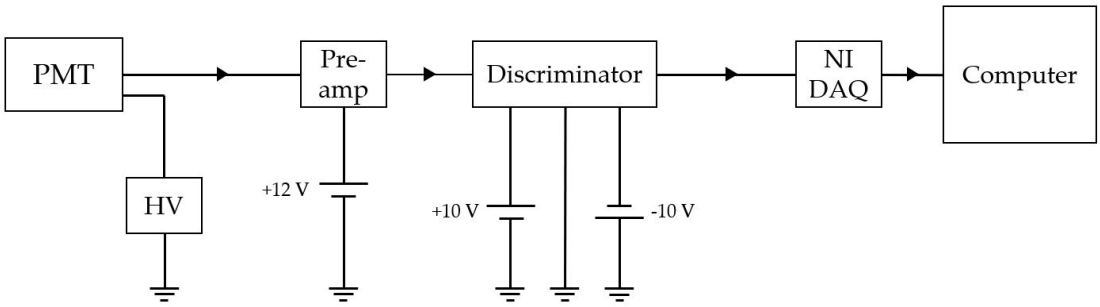

Figure 2.11: *Schematic of photon detection system. The high voltage power supply for the PMT is a Pacific Instruments model 204, and the other voltages are supplied by Topward 3303A DC power supplies.*

In addition to being able to measure the intensity of our light, we were able to characterize its polarization. The polarization of light can be completely described by four quantities known as the Stokes parameters. We can calculate these quantities by measuring the intensity as a function of the quarter-wave plate angular position and then taking a fast Fourier transform of our signal. This process is described in great detail in the paper by Berry et al. [13], and will be described further is Section 3.3. We created a program in LabVIEW that rotated the quarter-wave plate, recorded the intensity at each position, found the Fourier coefficients of our data, and calculated the relative Stokes parameters.

Chapter 3

Theory of Operation

In this chapter of the thesis, we will explain the principles by which the experiment operates, including the production of monochromatic electrons, the analysis of their energy, the production of light, and the measurement of optical properties.

3.1 The Trochoidal Monochromator

The electrons are produced from our tungsten filament via thermionic emission. This process usually requires running currents of about 4.5 A through the filament but can require more when chamber pressure is higher due to neon cooling the filament.

When the electrons are emitted from the filament, they are accelerated through the electrostatic lenses to the monochromator section where we have crossed electric (E) and magnetic (B) fields as shown in Figure 3.1. The magnetic field is along the axis of propagation and helps to keep the electrons collimated, and the electric field provides the transverse dispersion of our electrons. The force on the electrons in this region is given by the Lorentz force law

$$\vec{F} = -e(\vec{E} + \vec{v} \times \vec{B}), \tag{3.1}$$

where e is the fundamental charge of the electron, $\vec{E}$ is the electric field, $\vec{v}$ is the velocity of the electrons, and $\vec{B}$ is the magnetic field. If we assume that the electric and magnetic fields are both constants of magnitude E_o and B_o respectively, then Equation 3.1 can be separated into three dif-

ferential equations of which the x and y are coupled:

$$\ddot{x} = -\frac{eB_o}{m}\dot{y}, \tag{3.2}$$

$$\ddot{y} = \frac{eB_o}{m}\dot{x} - \frac{eE_o}{m}, \tag{3.3}$$

$$\text{and} \quad \ddot{z} = 0. \tag{3.4}$$

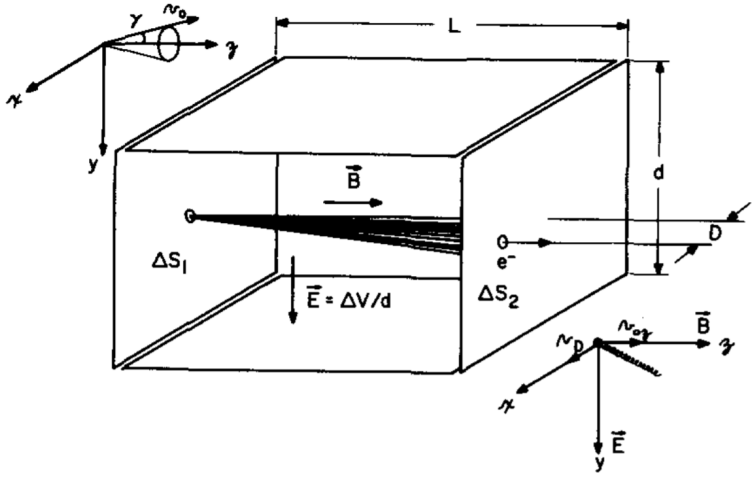

Figure 3.1: *Diagram of trochoidal monochromator with relevant parameters, taken from Roy [16]. Here, v_o is the initial velocity of the electron, γ is its initial angle with respect to the z axis, D is the separation of the entrance and exit apertures in the x direction, and ΔS_1 and ΔS_2 are the entrance and exit aperture diameters respectively.*

This system of differential equations can be solved quite easily, and the general form of the equations of motion are

$$x(t) = \frac{-(v_d - v_{ox})}{\omega}\sin(\omega t) + \frac{v_{oy}}{\omega}\cos(\omega t) + v_d t - \frac{v_{oy}}{\omega} + x_o, \tag{3.5}$$

$$y(t) = \frac{(v_d - v_{ox})}{\omega}\cos(\omega t) + \frac{v_{oy}}{\omega}\sin(\omega t) - \frac{(v_d - v_{ox})}{\omega} + y_o, \tag{3.6}$$

$$\text{and} \qquad z(t) = v_{oz} t, \tag{3.7}$$

where

$$v_d = \frac{E_o}{B_o} \quad \text{and} \tag{3.8}$$

$$\omega = \frac{eB_o}{m}, \tag{3.9}$$

with m being the mass of the electron. Note that the displacement velocity is independent of the charge so if we were dealing with protons or positrons the particles would tend to drift in the same direction. Also note that the angular frequency at which the electrons cycle is directly proportional to the strength of our magnetic field.

As shown in Figure 3.1, the entrance and exit holes of the monochromator are not concentric but rather a distance D apart. The electron travels the length L of the monochromator in time $t = L/v_{oz}$, and in that time the electron drifts an amount $x = v_d t$. For the electron to make it out of the monochromator, it has to drift exactly the distance $D = v_d t = v_d L/v_{oz}$ which means that it must have an initial velocity in the z-direction of $v_{oz} = v_d L/D$. This is essentially how the monochromator selects electrons with only certain energies. The drift velocity is determiend by the electric and magnetic field strengths that we apply, and only electrons of a certain velocity, and therefore a certain energy, can successfully traverse the monochromator. In reality, it is electrons within a certain energy range that can do this because the initial positions of the electrons as they enter the monochromator are not the same and because the exit aperture has a nonzero diameter allowing a range of velocities to be transmitted.

In practice there is usually an additional electric field in the z-direction created by the a voltage difference on M3 and M6, the plates before and after the monochromator section. If we add in the effects of this new field of strength E_1, we get

$$z(t) = \frac{\omega E_1}{2B_o} t^2 + v_{oz} t. \tag{3.10}$$

This means that in order for the electrons to drift just long enough to make it to the exit aperture they must have a velocity v_{oz} dictated by

$$D = \frac{E_o v_{oz}}{E_1 \omega} \left(\sqrt{1 + \frac{2\omega E_1 L}{B v_{oz}^2}} - 1 \right). \tag{3.11}$$

This equation returns the previous results for D in terms of v_{oz} in the limit of small E_1.

3.2 Retarding Field Analysis

When we have successfully created an electron beam by heating our filament enough and we think that it is monochromatized, we can check if it really is by performing a retarding field analysis. The idea behind this is that we create a larger and larger potential hill (see Figure 2.6 for an intuitive picture) for the electrons to climb up and measure the number that make it over. In practice, this means placing successively more negative voltages on the A2 and A3 deflector plates to create a retarding field and measuring the current on the main beam collector at each voltage, an example of which can be seen below in Figure 3.2. Ideally, we would see constant current until we reached a certain retarding field potential, at which point the current would drop to zero. This would mean that all the electrons had exactly the same energy. However, because the electrons are created with some initial energy distribution and because of the geometrical defects of our energy analyzer, the drop is spread out over a range of voltages. From this type of curve, we can infer the distribution of electron kinetic energies. However, as pointed out in [15], this type of energy measurement is somewhat inaccurate because it will only measure the distribution of momenta perpendicular to the retarding field and not the total kinetic energy of our electrons.

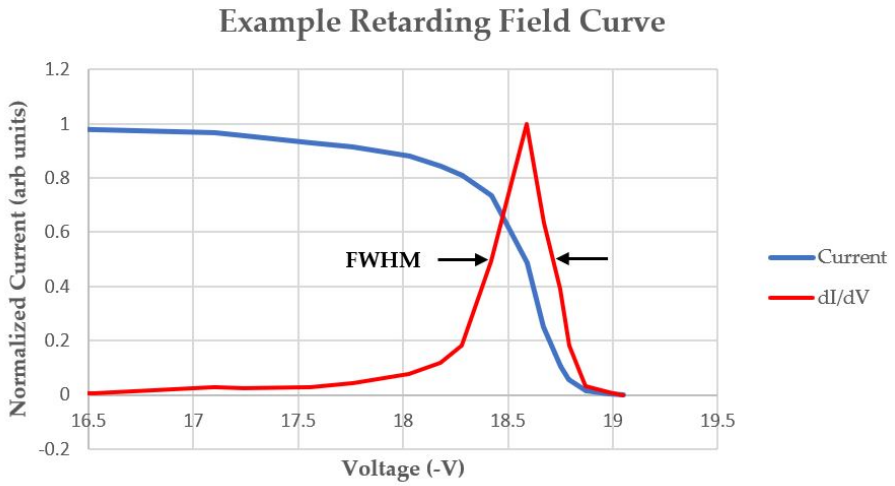

Figure 3.2: *Example of a retarding field curve with derivative showing the inferred energy distribution of the electrons. Current and derivative are normalized, and the full-width-half-maximum (FWHM) is indicated in the figure.*

3.3 Optical Polarization Measurements

When we have produced some light, we may want to know the state of its polarization. It is well known that the polarization state of light can be completely described by four parameters known as the Stokes parameters. They are defined as such [13]:

$$I = I(0°) + I(90°) = \left\langle |E_x|^2 \right\rangle + \left\langle |E_y|^2 \right\rangle, \tag{3.12}$$

$$M = I(0°) - I(90°) = \left\langle |E_x|^2 \right\rangle - \left\langle |E_y|^2 \right\rangle, \tag{3.13}$$

$$C = I(45°) - I(135°) = Re\left\langle E_x E_y \right\rangle, \tag{3.14}$$

$$\text{and} \quad S = I_{RHC} - I_{LHC} = Im\left\langle E_x E_y \right\rangle. \tag{3.15}$$

The electric field components E_x and E_y are in the x and y directions, and $I(\theta)$ is the intensity of light at the angle θ with respect to the x axis (see Figure 3.3). The brackets around the electric field components indicates a time average over many cycles, and I_{RHC} and I_{LHC} mean the intensity of right-handed and left-handed polarized light. A visual representation of the meaning of these parameters can be seen in Figure 3.3.

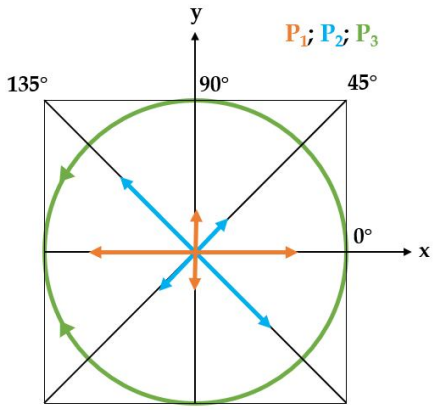

Figure 3.3: *Visual representation of the relative Stoke's parameters. Here $P_1 = M/I$, $P_2 = C/I$, and $P_3 = S/I$, where the orange P_1 is the linear polarization on the axes, the blue P_2 is canted linear polarization, and the green P_3 is the circular polarization of our light.*

To measure these parameters, we used a polarimeter as shown schematically in Ref. [13], (see Figure 3.4).

Given an input polarization state of (I,M,C,S), one can find the intensity of transmitted

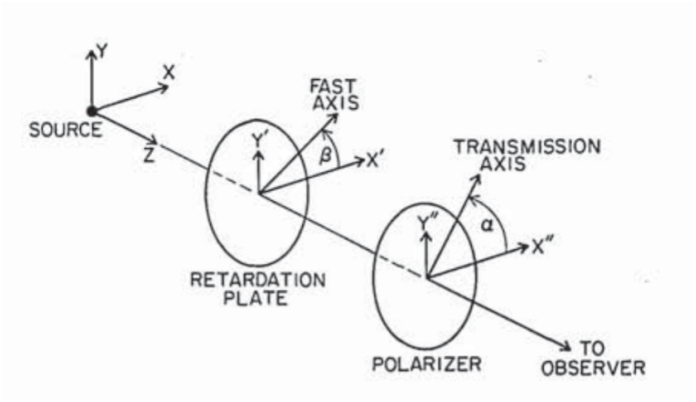

Figure 3.4: *Diagram of elements necessary for polarization measurements, taken from [13].*

light from the Mueller matrices for these optical elements. For a quarter waveplate that produces a phase difference of δ placed at an angle β and a linear polarizer placed at angle α, the transmitted intensity has the form [13]

$$I_T(\alpha,\beta,\delta) = \frac{1}{2}\left[I + \left(\frac{M}{2}\cos(2\alpha) + \frac{C}{2}\sin(2\alpha)\right)(1+\cos(\delta))\right] + \frac{1}{2}[S\sin(\delta)\sin(2\alpha-2\beta)] + \frac{1}{4}[(M\cos(2\alpha) - C\sin(2\alpha))\cos(4\beta) + (M\sin(2\alpha) + C\cos(2\alpha))\sin(4\beta)](1-\cos(\delta)). \tag{3.16}$$

Since we rotate the quarter-wave plate, we are changing the angle β. This means Equation 3.16 is essentially a function of $\cos(2\beta)$, $\cos(4\beta)$, $\sin(2\beta)$, and $\sin(4\beta)$ with a constant, or equivalently,

$$I_T(\beta) = C_o + C_2\cos(2\beta) + C_4\cos(4\beta) + S_2\sin(2\beta) + S_4\sin(4\beta). \tag{3.17}$$

If you have ever taken a class on partial differential equations, you would recognize that this is nothing but a partial Fourier series, and that taking the Fourier transform of this would give you the coefficients that we want to find. Once we have the coefficients, we can plug them into these equations provided by [13] to find the Stokes parameters for our light:

$$M = \frac{2}{1-\cos(\delta)}[C_4\cos(2\alpha+4\beta_o)+S_4\sin(2\alpha+4\beta_o)], \tag{3.18}$$

$$C = \frac{2}{1-\cos(\delta)}[S_4\cos(2\alpha+4\beta_o)-C_4\sigma(2\alpha+4\beta_o)], \tag{3.19}$$

$$S = \frac{C_2}{\sin(\delta)\sin(2\alpha+4\beta_o)} = \frac{-S_2}{\sin(\delta)\cos(2\alpha+4\beta_o)}, \tag{3.20}$$

$$\text{and} \quad I = C_o - \frac{1+\cos(\delta)}{1-\cos(\delta)}[C_4\cos(4\alpha+4\beta_o)+S_4\sin(4\alpha+4\beta_o)], \tag{3.21}$$

where β_o is the initial angle of the quarter wave plate with respect to the x axis. I created a program in LabVIEW that could rotate the quarter wave plate via stepper motor, take intensity measurements from the PMT at each position, find the Fourier coefficients of the resulting intensity curve, and calculate the Stokes parameters of our light. The front panel of this program can be seen in Figure 3.5.

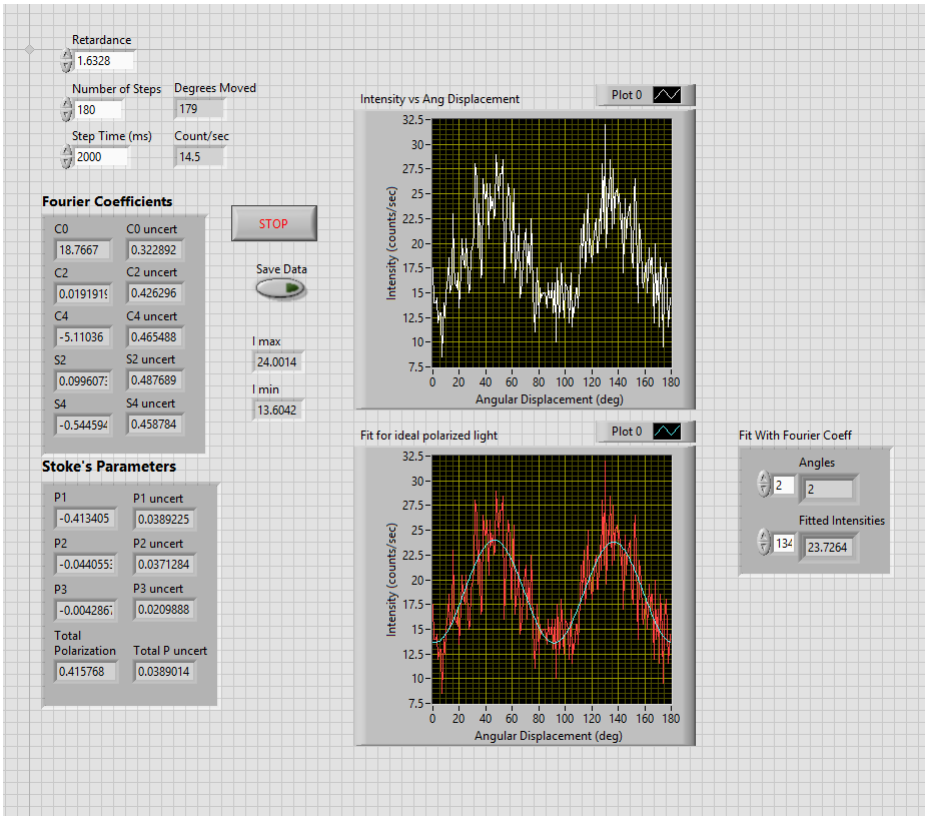

Figure 3.5: *Front panel of light analysis program. It was designed to display the intensity for each angle of the quarter wave plate (QWP) and, after all the data had been collected, display the measured data and the data with fit. The fit was displayed over the data as a visual check of the Fourier coefficients we calculated.*

Because we are not interested in the total intensity of our light for this measurement, we calculate the relative Stokes parameters which are defined as

$$P_1 = M/I, \tag{3.22}$$

$$P_2 = C/I, \tag{3.23}$$

$$\text{and} \quad P_3 = S/I. \tag{3.24}$$

These numbers all range between -1 and 1, and to find the total polarization for our light P_T, we simply add them in quadrature $P_T = \sqrt{P_1^2 + P_2^2 + P_3^2}$.

Chapter 4

Calibration

4.1 Optical Polarization Measurements

The first thing I did with the light analysis section was to disassemble it piece by piece, documenting all of the connections and how each of the pieces worked. After reassembling it, I acquired a neon discharge lamp from Dr. Keith Foreman to use as a test light source and designed the light analysis program that could rotate the stepper motors controlling the quarter wave plate position and take intensity measurements from the PMT. The quarter wave plate and the linear polarizer were rotated using Astrosyn Miniangle Stepper motors type 23LM-C304-15. The stepper motors would rotate a shaft with screw threading, and the threaded shaft was coupled to the toothed optics mount as can be seen in Figure 4.1. Both the optical mount and the drive shaft of the stepper motor were retractable via a plunger outside the housing so that we could take the element out of the beam line if desired. The gear ratio is such that the stepper motor must move 1000 steps to rotate the optical element 1 degree.

Next, we set up the neon discharge lamp in front of the north viewport of the vacuum chamber with a black piece of paper taped over it except for a small hole approximately 1 inch in diameter cut out as can be seen in Figure 4.2. This was the source of test light that we then passed through a converging lens of focal length 5 cm, a variable diameter iris, another converging lens of focal length 31 cm, and finally a sheet linear polarizer as can be seen in Figure 4.3. The first thing I did was to test Malus's law using the linear polarizer in front of the north viewport and the one inside the light analysis system. Malus's law says that the intensity of totally polarized

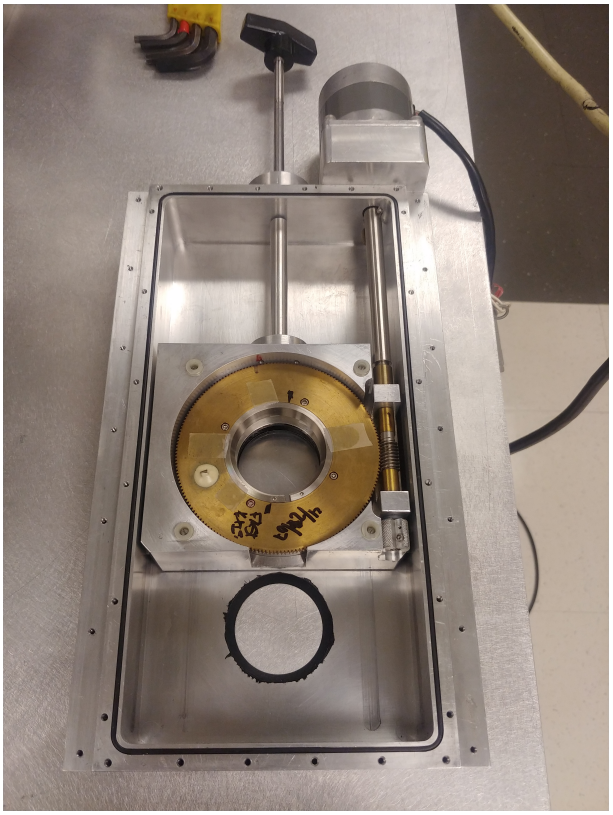

Figure 4.1: *Housing for the Meadowlark quarter wave plate displaying the rotation mechanism and plunger action.*

light I transmitted by a perfect linear polarizer is equal to the original intensity I_o times the cosine squared of the angle between the two polarization axes θ:

$$I = I_o \cos^2(\theta). \tag{4.1}$$

We set the initial linear polarization of our neon light using the first polarizer, and the polarizer controlled by our stepper motor acted as the analyzer. The fast axis of our sheet linear polarizer was determined by visual inspection of horizontally polarized light reflected from the floor tiles. Using this knowledge, we set the zero position of our analyzer to be horizontal. We then rotated the analyzer 1 degree at a time and recorded the count rate at each position. Figure 4.4 shows an example of this data. The top graph is the measured intensity in terms of counts, and the bottom graph is a fit of the data. This is in good agreement with the cosine squared dependence of Malus's Law.

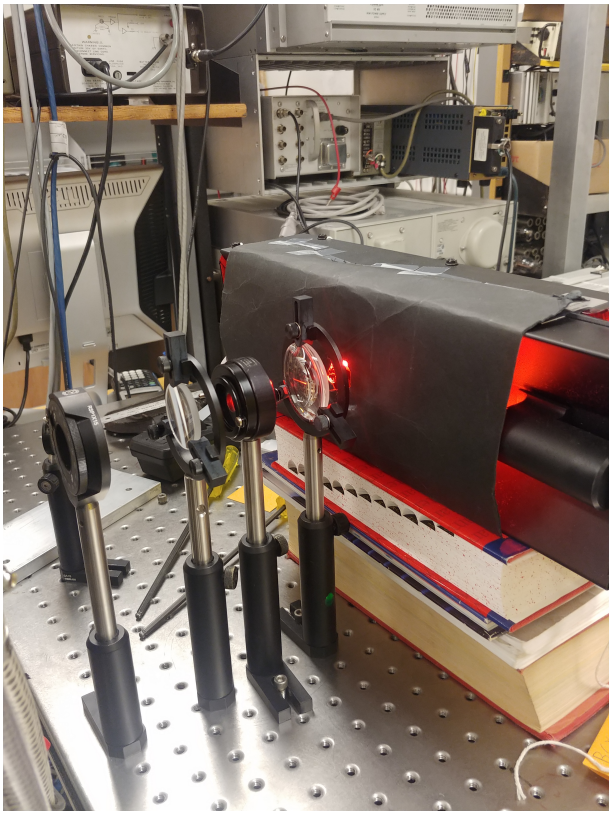

Figure 4.2: *Neon discharge lamp and optical train to simulate light being emitted from collision cell for testing light analysis system. Note that a hi-tech mounting system was used for elevating the discharge lamp.*

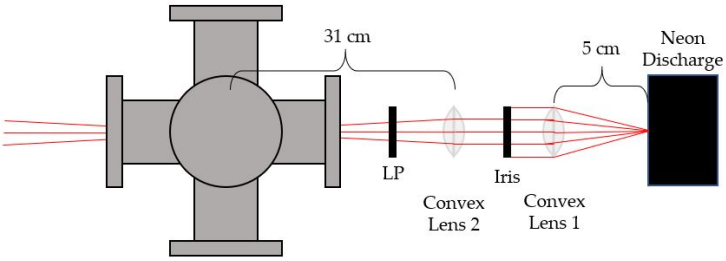

Figure 4.3: *Optics setup for testing light analysis system. Convex Lens 1 had focal length of 5 cm and was positioned 5 cm away from our source to collimate the light. The adjustable iris was used to vary the intentity. Convex Lens 2 had a focal length of 31 cm and was positioned 31 cm away from the center of the collision cell so that light appeared to be originating from the collision point.*

Having shown that we could reliably reproduce Malus's law using this system, we moved on to measuring the Stokes parameters for linearly polarized light. The goal was to be able to

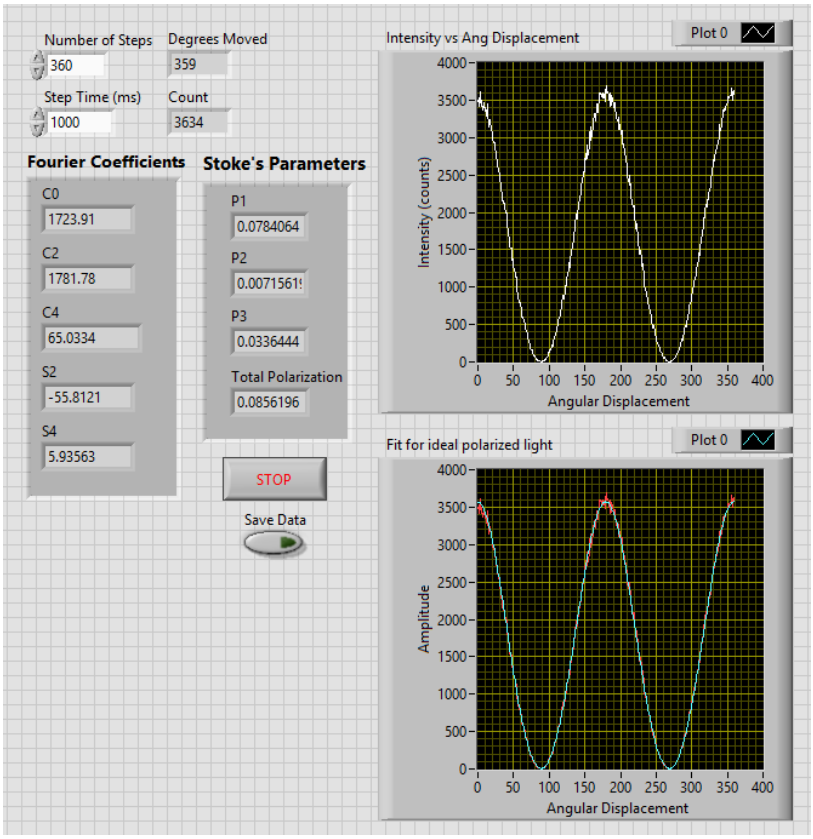

Figure 4.4: *Test of Malus's Law using two linear polarizers. Top graph is measured data, and bottom graph is data with a fit.*

have any orientation of linearly polarized light, measure the Stokes parameters for this light, and be able to determine what angle the polarizer was positioned at. I encountered some difficulties when starting this task, however. Setting up the code to calculate the Stokes parameters from our intensities measurements was relatively straightforward, but we had some confusing results regarding the total polarization of our light. We found that the total polarization depended on the angle at which we placed the polarizer, which went against common sense.

After testing whether this effect was due to the orientation of our neon discharge lamp, the quality of our polarizer, the nature of our interference filter, or extraneous background light, we found that the retardance we had been using to calculate the Stokes parameters was incorrect. The retarder that we had was a Meadowlark NQ-200-0468 designed to have a retardance of a quarter wave for 468 nm light. Since we were using 640.2 nm light, the retardance was actually 0.1652 as listed in the manufacturer's specifications for this optic. Rather than use this retarder, we decided

to use a Meadowlark BQ-200-0640.2 retarder which is designed for 640.2 nm light. The retardance listed in the specifications is 1.573 rad or 0.2503 waves, but we measured the retardance for our setup to be 1.632(8) rad. To measure the retardance, we first measured the extinction ratio K of our two linear polarizers with Equation 4.2.:

$$K = \sqrt{\frac{I_{max} - I_{min}}{I_{max} + I_{min}}}. \tag{4.2}$$

The extinction ratio is essentially a measure of how good our linear polarizers are at polarizing light. We measured our extinction ratio to be 0.9920(6). Next, we placed our retarder back in between the two polarizers, and measured the retardance δ using

$$\cos(\delta) = \frac{\frac{I_{min}}{I_{max}}(1 + K^2) - 1}{K^2}. \tag{4.3}$$

This method of measuring the retardance was provided to us by Dr. Keith Foreman.

Using this retarder and the measured retardance in our calculations of the Stokes parameters, we no longer saw the significant variation in the total polarization of our light. We measured the Stokes parameters for input linear polarization in a range of 180 degrees as shown in Figure 4.5. All parameters behaved as expected, except there is some slight variation of P3 and the total polarization. P3 is expected to be exactly 0, and the total polarization is supposed to be at or very close to 1 for all angles. The instabilities in these values could be due to a wobble of the gears as the retarder is rotated or perhaps slight misalignment of our optical elements. It could also, in principle, be due to a mis-calibration of the retardation. However, with this data in hand, we concluded that our light analysis system was in good enough working order and that we should move on to the production of electrons.

4.2 Production and Analysis of an Electron Beam

Similar to the beginning of looking at the light analysis system, we began looking at the electron gun by carefully taking everything apart and documenting the relevant connections. We started by taking the electron gun out of the vacuum chamber and using a Sperry DM-6400 multimeter to discern which feedthrough pins corresponded to which electrodes on the electron gun as well as to check for any shorts among the plates. The electrodes are stacked on top of each other with

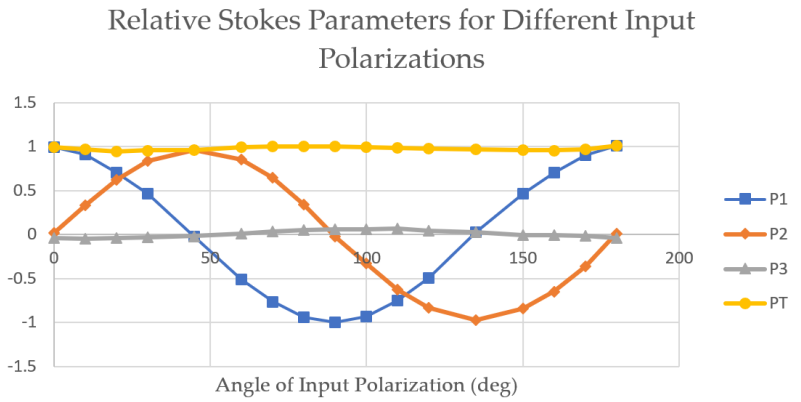

Figure 4.5: *Measurement of relative Stokes parameters for linearly polarized light as part of a test of the light analysis system.*

sapphire balls separating them so as to electrically isolate them.

After ensuring that all the connections were sound, we placed the electron gun back into the chamber and pumped it down. The next step was to figure out how to put voltages on each of the elements. Previous methods for doing this involved two power supply boxes crafted by Dr. Paul Burrow that acted principally as voltage divider circuits. One box was for the monochromator section leading up to the collision cell, and the other box was for the analyzing section after the collision cell. One voltage was generated, and we could control the voltages for each of the elements by using variable resistors. The circuit diagram for the monochromator box can be seen in Figure 4.6.

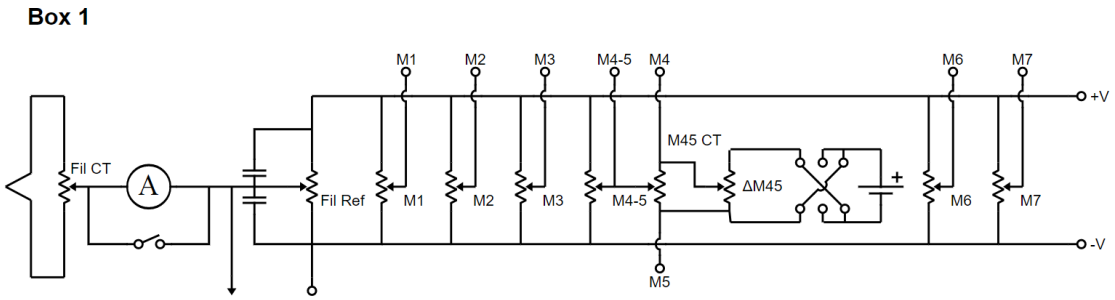

Figure 4.6: *Circuit diagram for the power supply box for the monochromator section of the electron gun. A resistor with an arrow next to it indicates a variable resistor. Voltages across variable resistors M1-7 all lead to plates M1-7 as shown in Figure 2.4.*

These power supply boxes have been fiddled with by many people attempting to under-

stand their internal workings or to fix them over the years, and so when we tried to use them to place voltages on the electron gun elements, it did not work reliably. We were able to place voltages on the elements, but they would vary over time and some of the variable resistors did not work. Thus, we decided to create my own setup for placing voltages on the electrodes. The simplest and easiest method was to grab many individual power supplies and rewire everything to them. Luckily, we had many small unused power supplies floating around in the lab, so we quickly purloined eleven of them and set them up as shown in Figure 4.7. In addition, we modified the panel on which all of the power supplies rest so that we could connect each of the voltages via BNC and it would collect all of them into two DB9 output connectors on the back, one for the monochromator voltages and one for the analyzer voltages. The schematic for these electrical connections is shown in Figure 4.8. This is a better system than the boxes because all of the voltages are referenced to ground which is simpler and more intuitive, it is easier to read off a given voltage profile for the electron gun, and it is more reliable. We can set the voltages, turn off all of the supplies, and leave for a week; when we get back, we measure the exact same voltages when we turn them back on. With this new voltage control method, we were ready to try producing a beam.

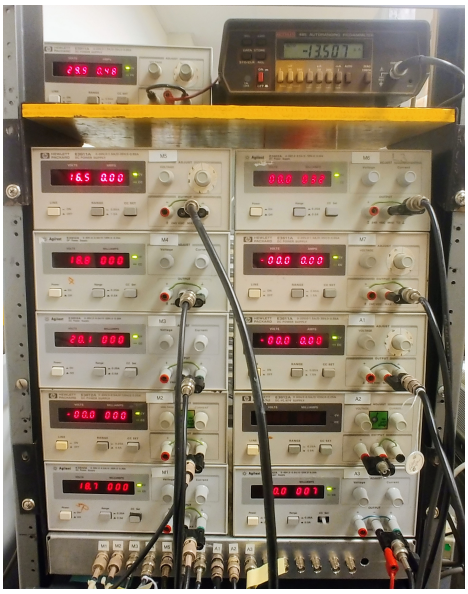

Figure 4.7: *Power supplies for controlling voltages on electrostatic elements in electron gun.*

Using a set of voltages recommended by Will Brunner to produce a narrow energy electron beam with the monochromator, we were able to get a transmitted (collector) current on the order of 1 nA. The voltages he suggested to us were determined from a simulation of the electron gun

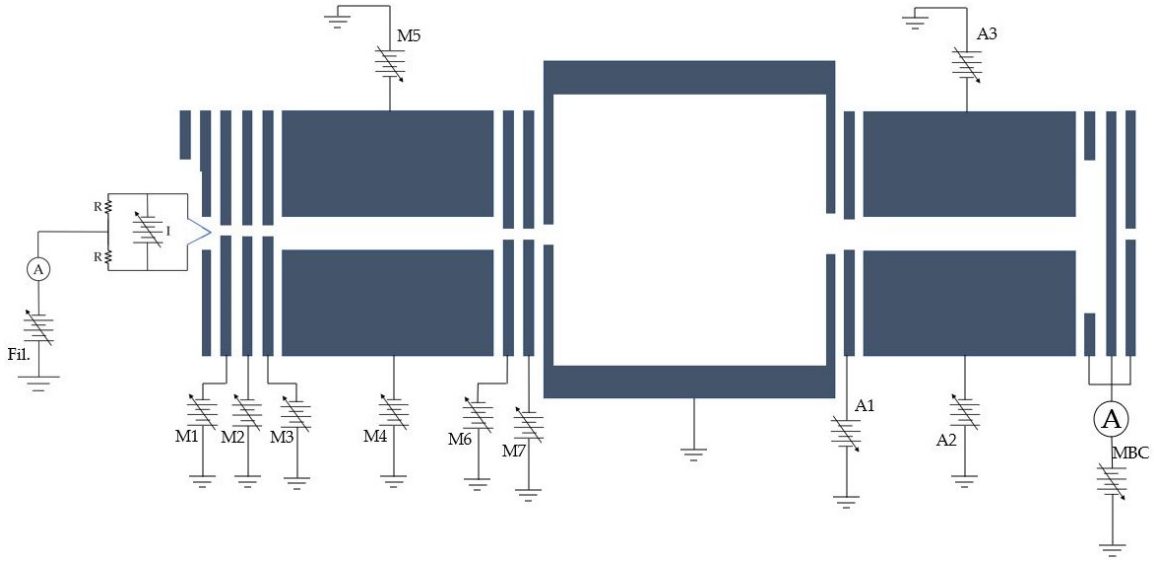

Figure 4.8: *Electrical schematic for how each of the elements if connected to a voltage.*

using the ray tracing software SIMION, and they are listed in Table 4.1.

Electrode	Voltage (V)
Fil	-18.5
M1	-18.4
M2	-18.3
M3	-18.2
M4	-18.85
M5	-18.35
M6	-17.7
M7	-18.0
CC	0
A1	0
A2	1.0
A3	1.0
MBC	27.5

Table 4.1: *Initial electron gun settings suggested by Will Brunner from SIMION simulations.*

Because we had successfully produced an electron beam using the power supply system that we made and voltages from SIMION, the next step was to measure the energy distribution of the electrons via retarding field analysis. Our initial idea was to place the retarding field on the collision cell, but this proved to be quite ineffective as it did not produce a well defined retarding voltage to stop the electrons. We thus decided to use the A2 and A3 half-cylinder ”plates” instead. This proved to be much better. We measured the current transmitted to the main beam collector as a

function of the voltage placed on A2 and A3, and fit this data with a complementary error function. A complementary error function is just the reflection of an error function across the vertical. From this fit, we were able to determine the full width half-maximum of our electron energy distribution and the center energy. The uncertainties on these parameters are given by the uncertainties in the nonlinear least-squares fit used in Matlab. The distribution is not necessarily Gaussian in nature, but based on visual inspection of the fit, we have some confidence that it is appropriate. This data and its fit can be seen below in Figure 4.9.

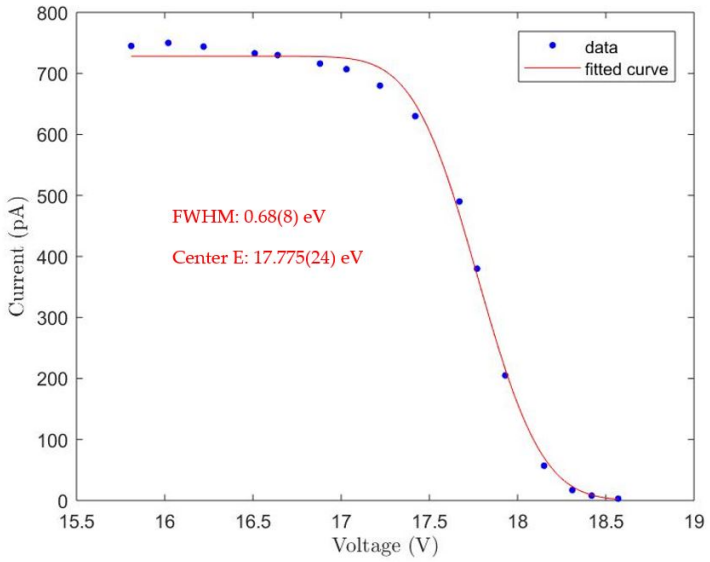

Figure 4.9: *Retarding field curve for electron beam produced with initial settings.*

To determine what we should expect for this measurement, we simulated, with the help of Will Brunner, a retarding field curve on A2 and A3 in SIMION, and we also looked at the true distribution of electron energies within the collision cell according to SIMION. To do this, we used the measured dimensions of the electron beam system to create a model in SIMION, and then, with all of the voltages specified in Table 4.1 on the corresponding simulated elements, we started 30,000 electrons from a point source at the filament tip. The electrons were created with an energy randomly sampled from a Gaussian distribution with mean energy of 0.4 eV and a FWHM of 0.275 eV. The initial angular distribution was a uniform cone with a half angle of 7.5 degrees. The electrons traveled through the monochromator region and to the retarding field on A2 and A3, and we counted the number of electrons that made it to the collector plate as a function of the voltage

on A2 and A3. To find the true energy of the electrons in the collision cell, we picked a point inside of it and told the program to record the kinetic energy of any electron that passed that point.

We suspected that the retarding field produced by A2 and A3 was not well defined, so we decided to include a simulation of the RFA with a wire mesh across A2 and A3. This is a common practice for producing a well defined retarding potential and is described in detail in [15]. The simulated retarding field curves were fitted with the same error function program used on actual measurements, and the true electron energy distribution was fit with a Gaussian profile shown in Figure 4.10. The uncertainties in the relevant parameters were taken from the fitting uncertainties in the program.

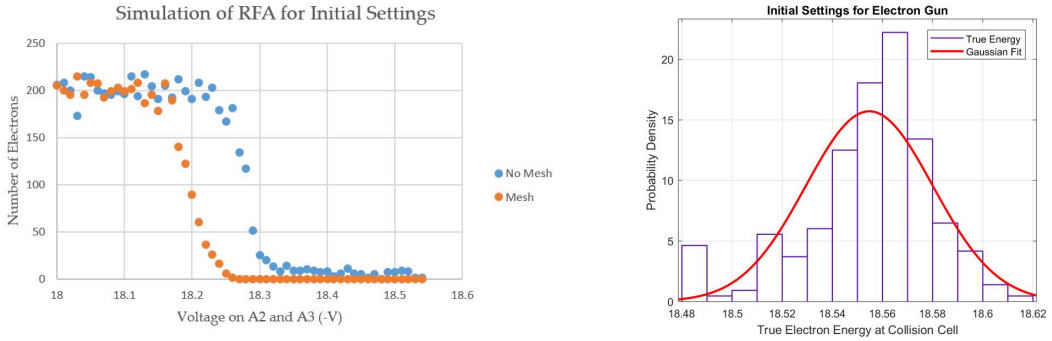

Figure 4.10: *(Left) Simulated RFA on A2 and A3 with and without a wire mesh. (Right) Distribution of electron energies at the collision cell using initial settings in Table 4.1. The data is from SIMION, and the Gaussian fit was made using Matlab.*

	Measured	**No Mesh Sim.**	**With Mesh Sim.**	**True**
FWHM (eV)	0.68(8)	0.046(8)	0.059(6)	0.060(3)
Center E (eV)	17.775(24)	18.279(1)	18.197(1)	18.555(2)

Table 4.2: *Comparison of measured and simulated retarding field analyses for initial settings listed in Table 4.1.*

The measured energy width was 0.68(8) eV wide which is about 11 times larger than the width of 0.060(3) eV predicted by SIMION for these settings. This is a large discrepancy that we do not have a good explanation for.

After weeks of tuning the settings on the monochromator and trying various methods of doing RFA, the best energy width we could measure was 0.410(26) eV. We did this by bringing M4 and M5 up 0.5 V, M6 up 3 V, and M7 all the way up to 0 V. The exact voltage settings are displayed below in Table 4.3, and the measured retarding field curve can be seen in Figure 4.11. Again, we

Electrode	Voltage (V)
Fil	-18.5
M1	-18.4
M2	-18.3
M3	-18.2
M4	-18.35
M5	-17.85
M6	-14.2
M7	0
CC	0
A1	0
A2	0
A3	0
MBC	27.5

Table 4.3: *Best electron gun settings for smallest measured energy width.*

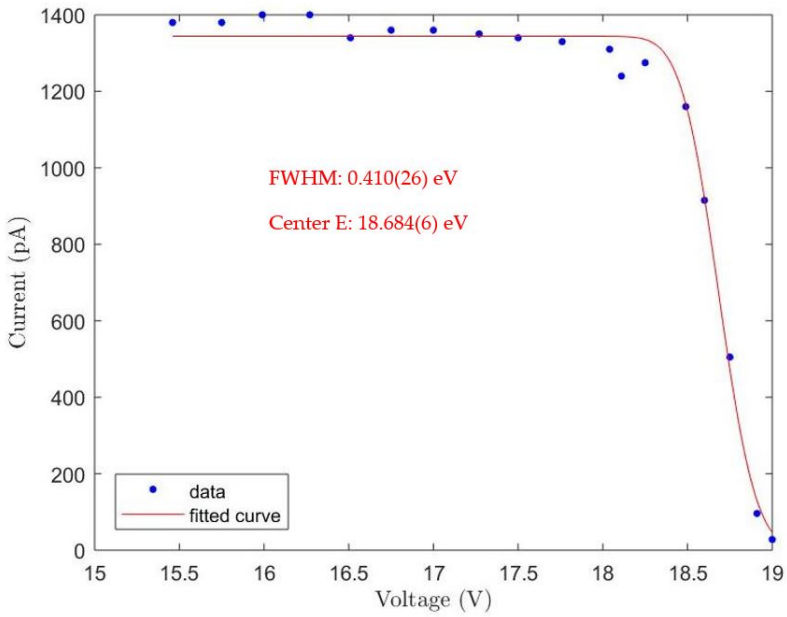

Figure 4.11: *Retarding field curve for best electron gun settings.*

wanted to compare our measurement to what SIMION could produce, so we simulated a retarding field curve using A2 and A3 with and without a wire mesh and recorded the true electron energy distribution within the collision cell shown in Figure 4.12. The simulated RFAs produced energy widths that were around half as large as the measured width.

We expected to be able to produce electron beams with energy widths on the order of 40 meV and transmitted currents on the order of 1 nA, but unfortunately, my experiments rarely

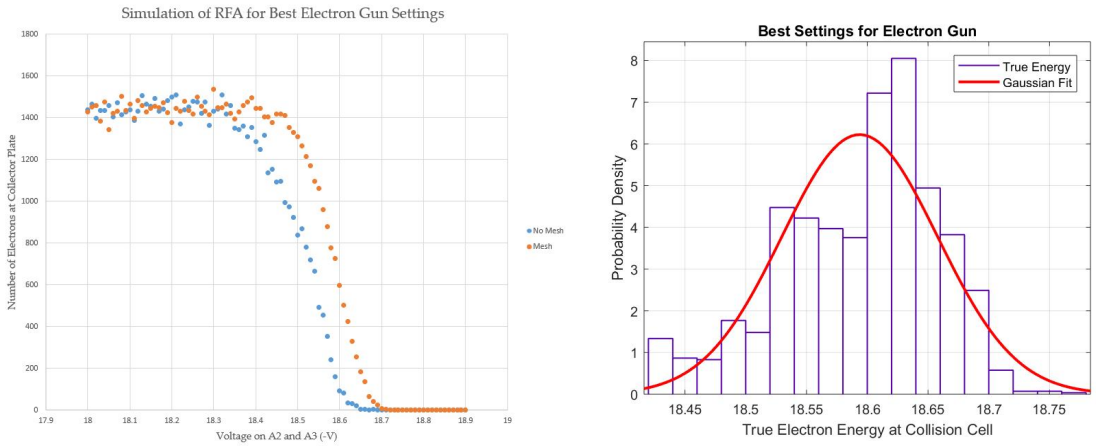

Figure 4.12: *(Left) Simulated RFA on A2 and A3 with and without a wire mesh. (Right) Distribution of electron energies at the collision cell using best settings in Table 4.3. The data is from SIMION, and the Gaussian fit was made using Matlab.*

	Measured	**No Mesh Sim.**	**With Mesh Sim.**	**True**
FWHM (eV)	0.410(26)	0.181(13)	0.141(7)	0.151(3)
Center E (eV)	18.684(6)	18.516(1)	18.585(1)	18.594(2)

Table 4.4: *Comparison of measured and simulated retarding field analyses.*

worked like the simulations. It is possible that the true voltages on the elements were not exactly the same as those we used in the simulation, or that the current supplies for the filament and magnets were not constant, changing the initial electron energy distribution or the strength of the magnetic field. We also assumed in the simulation that the magnetic field was constant in magnitude along the length of the electron gun. That is not the most accurate picture because according to theory and measurements on similar setups, it should dip in the middle. One thing we did learn from this study was that we could improve our retarding field curve measurements by adding a wire mesh across A2 and A3 because the simulated RFA with the mesh was always closer to the true width than the one without the mesh.

Because our measured energy width was so much larger than the expected one, we sought other means to quantify the spread in our electron energy distribution. Therefore, we looked to the resonances of neon and the excitation function of the $2p^5 3p\ ^3D_3 \rightarrow 2p^5 3s\ ^3P_2$ 640.2 nm transition. The excitation function as measured by Trantham et al. can be seen below in Figure 4.13 [14]. If our electron beam were actually monochromatized we would be able to reproduce this curve with more detail, and we could measure the energy width of our beam because the width of the feature

around 19 eV should just be the quadrature sum of our electron beam width and the natural width of the resonance 30 meV found in [4].

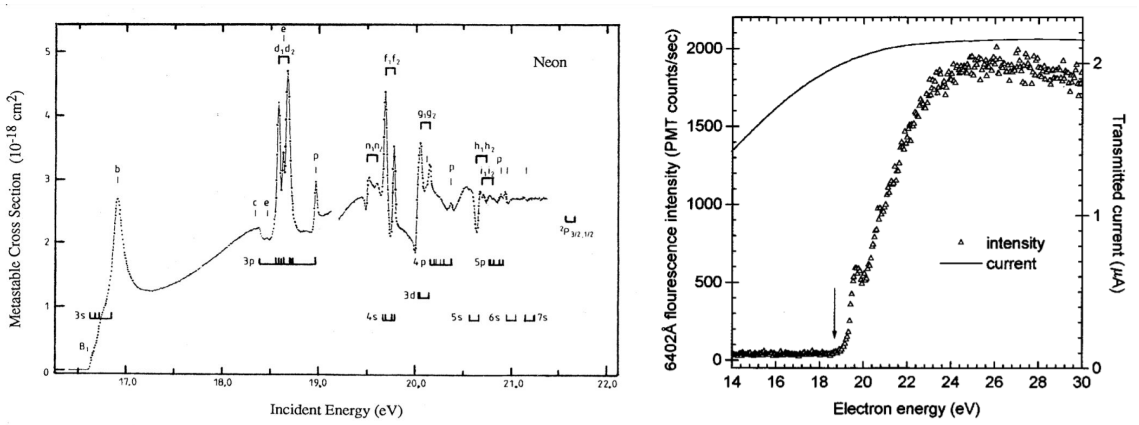

Figure 4.13: *(Left) Cross section of neon as a function of energy displaying resonances, taken from [4]. (Right) Excitation function for the $2p^5 3p\ ^3D_3 \rightarrow 2p^5 3s\ ^3P_2$ 640.2 nm transition in neon taken from [14]. The estimated ΔE for the incident beam in these measurements was approximately 300 meV.*

4.3 The Search for Light

We began our search for light from the neon resonance by rescuing our group's compressed cylinder of research grade neon gas from the Advanced Lab on the second floor of Jorgensen Hall and connecting it to our valve manifold. We then determined how the number of turns on our Granville-Phillips series 203 leak valve changed the chamber pressure which can be seen in Figure 4.14. The y axis is plotted on a logarithmic scale.

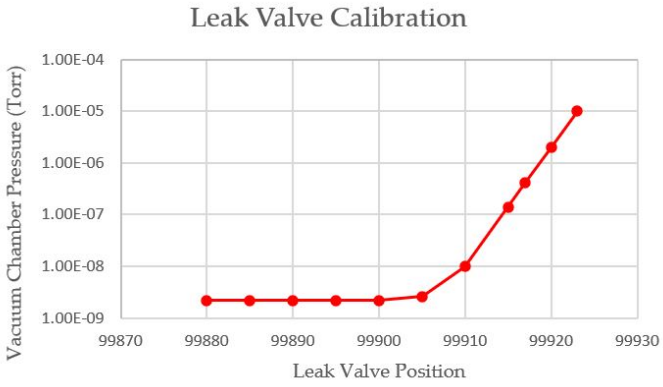

Figure 4.14: *Calibration of the leak valve for metering neon into the system.*

The next step was to introduce an amount of neon into our system, produce an electron beam that we think is monochromatized, and look for light above background with our PMT. We did have to be careful when adding in the gas to our system because it would have the effect of cooling down our filament, thus lowering our emission current and overall transmitted current. To overcome this obstacle all that was required was increasing the heating current for our filament. This generally meant increasing the heating current by around 0.5 A (4.5 A to 5.0 A) for pressures around 1×10^{-6} Torr.

However before we could look for light from the neon excitation and resulting decay, we had to discern what our sources of background light were and if we could reduce them. We determined that the filament of the ionization gauge was a significant source of background light that was horizontally polarized (P1 = 0.436(44)). This makes sense because it is a source of light directly above the cylindrical electron gun collision cell, so light that bounced off this and progressed to the PMT would be horizontally polarized due to Fresnel's equations. We easily removed this by turning off the ion gauge when doing intensity measurements.

The next and predominant source of background light came from the white-hot tungsten filament producing our electrons. This can be seen in Figure 4.15. Background light from this is unavoidable because of the current design of our electron gun. We cannot reduce the heating current; otherwise we would lose our electron beam. Moreover, we can't block the light without taking out the electron gun and modifying it in some way. Thus, we have to measure and subtract this intensity from all of our measurements.

For a chamber pressure of 3×10^{-9} Torr, no voltages on any of the elements, the PMT set to 1700 V, and the discriminator LLT set to -180.4 mV, we measured the intensity of light reaching the PMT as a function of heating current. In addition, we measured this while the ion gauge was off and a black cloth was covering the north viewport. This data can be seen in Figure 4.16.

To look for any light above this background when we had neon and an electron beam in the system, we needed to deflect the beam, measure the background, put the beam back into the neon, and measure the signal plus background. We initially tried this with a chamber pressure of 2×10^{-7} and a transmitted current of 1 nA because that was the best transmitted current we had achieved up to that point. At these settings, we didn't see any light above background, so we increased the chamber pressure and learned to increase the transmitted current by more than two orders of magnitude. With a chamber pressure of 1.0×10^{-5} Torr and transmitted currents greater

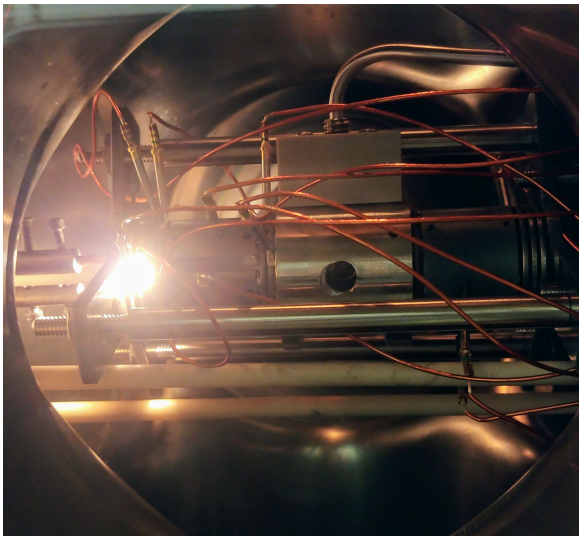

Figure 4.15: *Light emitted from the hot tungsten filament as seen through the north viewport of the vacuum chamber. Heating current is approximately 5.0 A.*

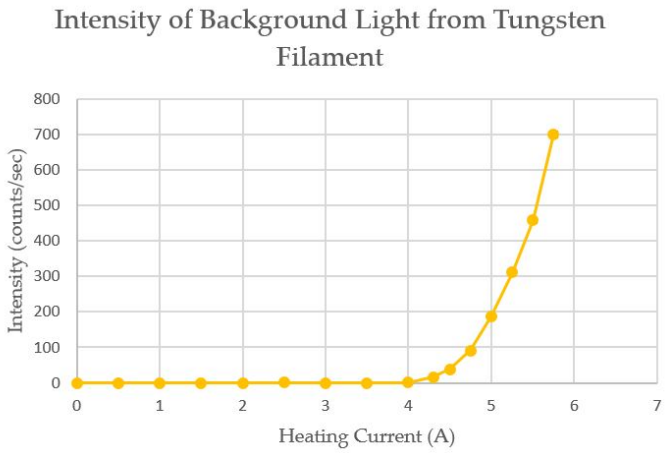

Figure 4.16: *Intensity of light from the filament as we change heating current.*

than 100 nA, we still did not see anything appreciably larger than the background light. We were able to increase the transmitted current by increasing the voltage on M1 which produced more electrons from our filament by field emission and also by increasing M4 and M5 (making them less negative).

The data shown in Figure 4.17 is problematic because we expect to see some amount of light at such high currents. There must thus be something wrong with our system. One possible cause of this failure to see light is that we are not properly deflecting the electron beam when

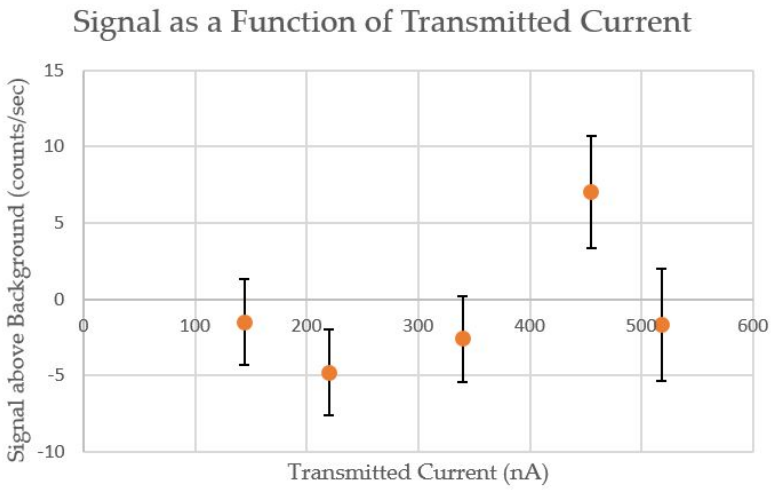

Figure 4.17: *Light above background as a function of transmitted current through the electron gun.*

making background intensity measurements. This would mean that our "background" and our signal plus background measurements were the same. To test this idea, we measured the current on the gas needle with and without the beam being deflected. For an emission current of 1.2 μA, we measured a current of 0.5 nA with the beam on course, and with the beam deflected using a strongly negative voltage on M6 and M7, we measured 0 nA. We also saw a similar reduction to 0 nA on all the electrodes in the analyzer when deflecting the beam this way. This indicates that we were definitely deflecting the electron beam and rules out that theory for why we are not seeing any light above background.

Next we thought that perhaps the electron beam was being clipped by the gas needle so we decided look for light above background as a function of the voltage placed on the gas needle. We placed voltages ranging from +9 V (attracting electrons to the tip) to -9 V (repelling electrons from the tip). As can be seen in Figure 4.18, this did not yield any positive results either.

Later, when disassembling the light analysis system to check the collimating lens, we discovered that the electron beam electrode-assembly was inserted into the vacuum chamber slightly rotated about the beam axis so that the fluorescence exit aperture on the collision cell was angled down instead of pointing directly towards the collimating lens. In addition we discovered that the collimating lens is preceded by a cone to block out background light and that the exit aperture on the collision cell is not concentric with the cone entrance hole shown in Figure 4.19. It is displaced from the cone's center by about 0.4 cm. I quickly corrected the downward tilt of the exit aperture,

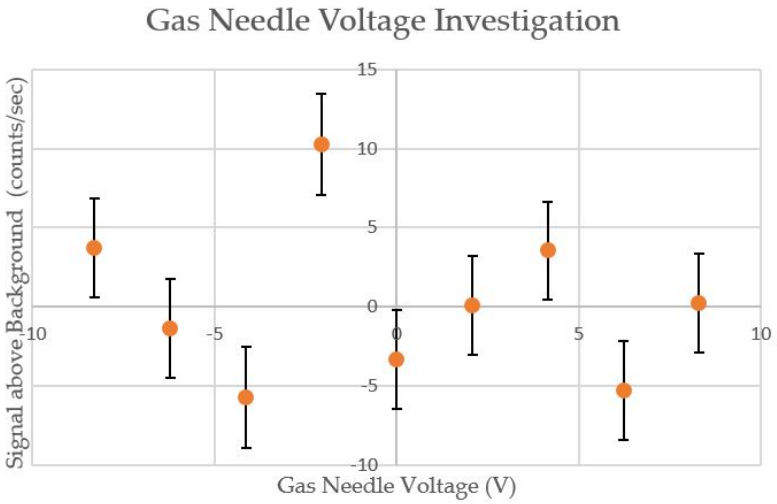

Figure 4.18: *Looking for light above background as a function of voltage placed on the gas needle.*

but we unable to correct the displacement from the cone center because that would require adding spacers to the electron gun stack. After rotating the electron gun so that the collision cell aperture was horizontal, we still did not see any non-background fluorescent light. The next thing we could try to do to see light would be to rotate the whole electron gun 90 degrees so that the large square hole on the bottom of the collision cell would be facing the cone hole.

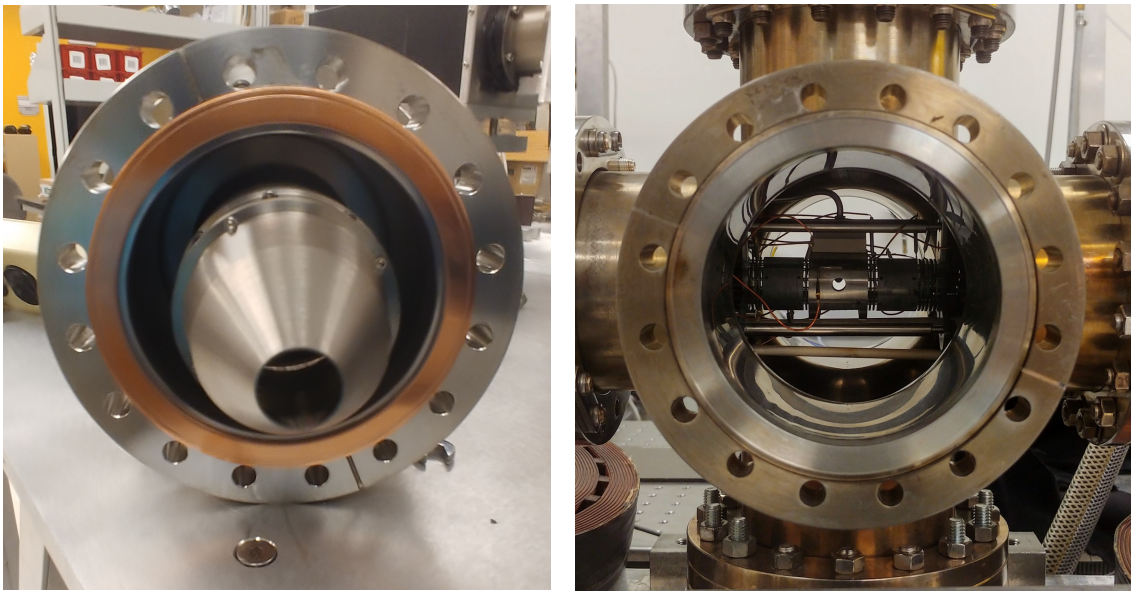

Figure 4.19: *(Left) Cone preceding collimating lens for light analysis system. (Right) Electron gun from the view of the south viewport where the collimating lens cone goes.*

Chapter 5

Conclusions

We have made great strides over the course of this project. We successfully created a beam of electrons, we measured the degree of monochomatization of the beam and compared it to SIMION simulations, and we analyzed the sources of light being emitted from our collision chamber. We learned that although we can produce electron beams with energy widths as small as 400 meV, our method of doing retarding field analysis is imperfect and that there are unknown complications that make our results worse than our simulations. We learned from simulation that adding a mesh across the A2 and A3 plates would make our retarding field curves slightly better. We learned that the largest source of background light in our system is the hot tungsten filament, and that with the current setup it is unavoidable in our measurements.

Despite all these things that we learned about this experiment, there are still many things that can be done to improve its functioning. In order to make our simulation of the electron gun better, we need to know more about the energy distribution of the electrons being emitted from the filament. To get this information we need to be able to measure the temperature of the filament. We could do this by perhaps attaching a thermocouple to the filament or near the filament and connecting it to one of the electrical feedthroughs or perhaps by measuring the change in resistance of the filament to infer its change in temperature. Another thing we can do to improve our simulation of the gun is to measure the magnetic field throughout the entire system at different magnet supply currents. This has not been done yet and for our simulations we have assumed that the magnetic field is constant throughout and equal to 80-100 Gauss. We also need to verify that the dimensions of the electron gun used in our simulation are correct. To find the dimensions initially we had what

we think is an exact replica of the electron gun and measured those. However, we did not measure the dimensions on the one currently in the vacuum chamber.

To improve our method of retarding field analysis we could add a wire mesh across plates A2 and A3 to make a more well-defined retarding potential, and we could find some way to automate the process of making retarding field curves because the current method is very time consuming. We could get a power supply that can be remotely controlled and connect both that and the electrometer to the computer. Then we could make a program that would change the voltage, record the current, plot the result, fit it, and calculate the energy width automatically. With this, we could more efficiently explore the parameter space for the electron gun to find the settings that produce the best energy widths.

To improve our chances of seeing light from neon with our PMT, we should first try rotating the electron gun 90 degrees so that the cutout on the bottom of the collision cell for gas to escape is facing the collimating lens. This cutout is larger than the exit aperture on the side and maybe this will allow light to get all the way through to the PMT. In addition, we could create some black shielding to block or absorb the light coming from the hot filament. This would reduce our background and increase our chances of seeing statistically significant intensities above background. We should also add some spacers in the electrode stack so that the exit aperture on the collision cell is concentric with the collimating lens.

Bibliography

[1] Schulz, G. J. *Resonances in Electron Impact on Atoms*. Review of Modern Physics Vol 45, No. 3. (1973)

[2] Fano, U. *Excitation of atoms to states of high orbital momentum.* Journal of Physics B: Atomic and Molecular Physics, Vol. 7, No. 14. (1974).

[3] Feshbach, H. *The unified theory of nuclear reactions: III. Overlapping resonances*. Annals of Physics, Vol. 43, Issue 3, (1967)

[4] Buckman, Stephen J. and Clark, Charles W. *Atomic Negative-Ion Resonances.* Review of Modern Physics, Vol. 66, No. 2. (April 1994).

[5] Sullivan J. P., Gilbert S. J., Marler J. P., Greaves R. G., Buckman S. J., and Surko C. M.. *Positron Scattering from atoms and molecules using a magnetized beam.* Physical Review A 66, 042708 (2002).

[6] Stamatovic, A. and Schulz, G. J. *Trochoidal Electron Monochromator.* Review of Scientific Instruments 39, 1752 (1968). DOI: http://dx.doi.org/10.1063/1.1683220

[7] Maseberg, J. W., Bartschat, K., and Gay, T. J. *Threshold Alignment Reversal and Circularly Polarized Fluorescence in Rotationally Resolved H_2.* Physical Review Letters 111, 253201 (2013). DOI: http://dx.doi.org/10.1103/PhysRevLett.111.253201

[8] Gay, T. J., Furst, J. E., Trantham, K. W., and Wijayaratna, W. M. K. P. *Optical Electron Polarimetry with Heavy Noble Gases.* Physical Review A. Vol. 53, No. 3. pp. 1623-1629. (1996)

[9] Davisson, C. and Germer, L. H. *The Thermionic Work Function of Tungsten.* Physical Review Journals Archive Vol. 20, No. 300 Published (1 Oct, 1922). DOI: https://doi.org/10.1103/PhysRev.20.300

[10] Pirbhai, M. H. *Optically-Pumped Spin-Exchange Polarized Electron Source*. PhD. Dissertation. University of Nebraska-Lincoln (2013).

[11] *TMP/NT-150/360 Turbomolecular Pump & Frequency Converter Manual*. Leybold Vacuum Products Inc. Part Number 99-800-010. Edition E.

[12] *Series 203 Granville-Phillips Variable Leak Valve*. Instruction Manual. Part number 203026. Revision B (November 2016).

[13] Berry, H. G., Gabrielse, G., and Livingston, A. E. *Measurement of the Stokes Parameters of Light.* Applied Optics. Vol. 16, No. 12. (December 1977).

[14] Trantham, K. W., Gay, T. J., and Vandiver, R. J. *An Inline Optical Electron Polarimeter.* Review of Scientific Instruments. Vol. 67. No. 12. (December 1996).

[15] Simpson, J. Arol. *Design of Retarding Field Energy Analyzers.* Review of Scientific Instruments. Vol. 32, No. 12. (December 1961). DOI: https://doi.org/10.1063/1.1717235

[16] Roy, D. *Characteristics of the Trochoidal Monochromator by Calculation of Electron Energy Distribution.* Review of Scientific Instruments, Vol. 43, No. 3. (March 1972).